Politecnico di Torino

Master's Degree in Aerospace Engineering

Academic year 2024-2025

Master's degree thesis

Analysis of far-field thermodynamics formulation for drag decomposition in unsteady flows

Supervisors

Domenic D'AMBROSIO

Manuel CARRENO RUIZ

Candidate

Andrea Angelo FRANCO

Abstract

An aerodynamic engineer must develop solutions to reduce drag, create more efficient aerodynamic devices and decrease fuel consumption to achieve a sustainable project.

A CFD solver can break down aerodynamic drag into two main phenomena. It computes the pressure field and shear stresses at the walls, then integrates these values over the body. However, the engineer must understand the specific sources of these phenomena.

In addition to drag computation at the wall, known as the near-field method, far-field methods have been studied since the early 20th century to capture more phenomenological information, such as drag due to viscosity, shock waves and induced effects.

This study will analyze a specific unsteady far-field method developed by Toubin, implemented in StarCCM+. It is a momentum-based approach with a thermodynamic formulation for far-field drag decomposition in unsteady flows, focusing also on the definitions of domains where the sources of drag occur. Several test cases are conducted to assess each drag contribution individually and then examine their interactions.

Contents

List of Figures

List of Tables

Chapter 1

Far-field methods and thermodynamic formulations for drag decomposition

1.1 Context

The aerospace industry is increasingly committed to finding solutions to reduce fuel consumption, driven by regulatory pressures and growing environmental awareness. These goals are translating into studies of lighter materials, more efficient engines and reduced drag to improve aircraft efficiency.

In this context, the aerodynamic engineer plays a fundamental role by analyzing and optimizing external surfaces. Analyses can be carried out experimentally or numerically. Experimental techniques have been used for a long time and are reliable, but they require significant economic and time resources, especially when multiple designs need to be studied. With the ever-growing availability of computational power, CFD methods are increasingly used, appropriately validated by wind tunnel measurements.

CFD simulation is a numerical technique that allows the analysis of fluid behavior by solving the governing equations. Drag estimation can be performed in two ways. The simplest method is the near-field method. The pressure field and wall shear stresses are evaluated, integrated, and the component parallel to the freestream flow is extracted.

In the early 20th century, another type of drag calculation was developed, known as the far-field method. The underlying idea of far-field methods is to apply conservation laws on control volumes that enclose the body. With regard to drag calculation, these methods allow the drag to be calculated by integrating far from the body, rather than on its surface.

This idea has another fundamental advantage. If the integration domains enclose the sources of drag, such as a shock wave, the boundary layer, and the wake, it is possible to break down the aerodynamic drag into the various contributions of each physical phenomenon. This makes far-field methods particularly interesting from a research perspective.

With this idea, the total drag is decomposed by phenomenon. In particular, the splitting of the total drag involves the definition of three types of drag:

Viscous drag is the portion of drag generated by the viscous friction produced in the boundary layer and in the wake.

Wave drag is the portion of drag due to the formation of a shock wave.

Induced drag is the portion of drag due to the local variation of the angle of attack caused by the spatial and temporal variation of lift (wingtip vortex and vortex shedding).

The far-field methods initially studied were based on steady flows. The first formulation for unsteady flows only appeared in 2013, with the studies conducted by Gariépy [4]. In that work, an in-depth study was carried out on the formulation proposed by Toubin [12], where Gariépy's theory is improved and two other sources of drag are taken into account. After an in-depth analysis of Toubin's proposed theory, another decomposition was studied and compared with Toubin's in the different cases analyzed.

1.2 Far-field methods

Several drag breakdown methods have been studied to date. This thesis will analyze a decomposition based on a thermodynamic formulation, where quantities such as entropy, total enthalpy, and pressure are used for the calculation and breakdown of aerodynamic drag. There are other methods based on a purely energetic formulation, and others based on velocity and vorticity vectors [13].

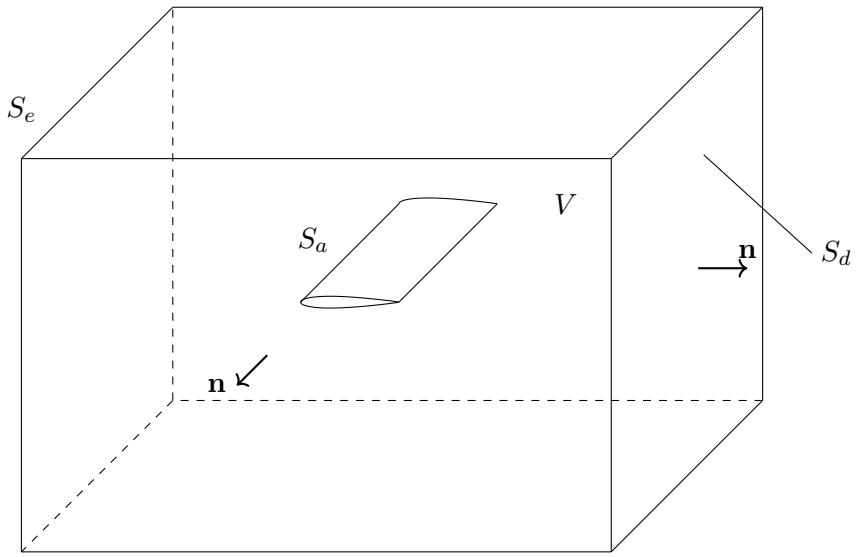

Figure 1.1: Definition of far-field domain and normal direction. The normal on surface S_a point inside the wing.

1.3 Steady formulations

The first far-field methods were developed for steady flows only. The first method was proposed by Betz in 1925. Several formulations followed, but drag decomposition was still incomplete as a formulation for induced drag was missing. It was not until 1972 that the first formulation for induced drag was developed.

1.3.1 Betz formulation

Betz introduced the first method of far-field drag decomposition [1]. Through experimental measurements carried out on the wake, on a plane downstream of the airfoil, it is possible to evaluate the profile drag. However, the induced drag was still calculated using the approximation for a finite wing with an elliptical planform. The profile drag was obtained by subtracting the induced drag from the total calculated drag.

In a wake plane S_d sufficiently far from the body, it can be assumed that the flow is aligned with the free stream and that the variation in total temperature is negligible. Therefore, the assumptions in the wake plane are

$$v = w = 0 \qquad\qquad T^\circ = T^\circ_\infty \,.$$

The formulation found by Betz is

$$D_{vw}^{Betz} = \int_{S_d} (p^\circ_\infty - p^\circ)\,\mathrm{d}S - \frac{\rho}{2}\int_{S_d} (u' - u)(2u_\infty - u' - u)\,\mathrm{d}S$$

where u' is the axial velocity that a potential flow would have in the same study case. His formulation is valid only for incompressible flows, so $p^\circ = p + 1/2\rho u^2$. In his study, Betz states that the second integral is negligible compared to the first.

1.3.2 Jones formulation

Jones' formulation [6] uses more restrictive assumptions to eliminate the second integral term present in Betz's formulation. He assumes that in the wake plane, the pressure is homogeneous and equal to the free-stream pressure, and that the velocity is aligned with the freestream velocity, so that in S_d the following hold:

$$v = w = 0 \qquad\qquad p = p_\infty \,.$$

With these assumptions, Jones' formulation is

$$D_{vw}^{Jones} = p_{d\infty} \int_{S_d} 2\sqrt{p_d^* - p^*}(1 - \sqrt{p_d^*})\,\mathrm{d}S$$

where

$$p_d = p^\circ - p = \frac{1}{2}\rho u^2$$

is the dynamic pressure and p_d^* and p^* are the dimensionless dynamic and static pressures, normalized by the dynamic pressure of the free stream $p_{d\infty}$. Again, this formulation is valid only for incompressible flows.

1.3.3 Oswatitsch formulation

Oswatitsch developed the first formulation based on thermodynamic considerations [9]. He starts from a momentum balance on the wake plane for the drag component and neglects the friction forces, thus

$$D = \int_{S_d} u_\infty \, \rho_\infty \, (u - u_\infty) + (p - p_\infty) \, (\boldsymbol{i} \cdot \boldsymbol{n}) \, \mathrm{d}S$$

With the assumption that the mechanical work on the fluid is zero and that there are two thermodynamic states that differ slightly from the initial state, we have

$$\delta Q = \delta E \qquad \Rightarrow \qquad T_\infty \, \rho \, (s - s_\infty) = \rho \, e = \rho \, (h - h_\infty) - (p - p_\infty) \, .$$

Substituting this relation into the first and neglecting friction work and heat conduction on the control surface S_d, we get the following.

$$D_{vw}^{Oswatitsch} = \frac{T_\infty}{u_\infty} \int_{S_d} \rho u \Delta s \, \mathrm{d}S = \frac{T_\infty}{u_\infty} \int_{S_d} \rho \, u \, s \, \mathrm{d}S$$

1.3.4 Maskell formulation

Maskell was the first to propose an expression for induced drag [7]. Using the total pressure, he obtained an expression for the total drag. His expression for profile drag is very similar to Betz's, except for a correction term u_b to account for the blocking effect in the wind tunnel facility.

$$D_{vw}^{Maskell} = \int_{S_d} (p_\infty^\circ - p^\circ) \, \mathrm{d}S + \frac{\rho}{2} \int_{S_d} (u' - u)(u' + u - 2(u_\infty + u_b)) \, \mathrm{d}S$$

In terms of induced drag, the stream function ψ, the potential velocity ϕ, the axial vorticity $\zeta = \partial w / \partial y - \partial v / \partial z$ and the source term $\sigma = \partial v / \partial y - \partial w / \partial z$ are used.

$$D_i^{Maskell} = \rho \int_{S_d} (v^2 + w^2) \, \mathrm{d}S = \rho \int_{S_d} (\psi \zeta - \phi \sigma) \, \mathrm{d}S$$

1.3.5 Van der Vooren and Desterac formulation

In this formulation, both assumptions on the wake plane and the thermodynamic expression for the axial velocity are applied. If the mass and momentum balance in the freestream flow direction are applied in the volume V from figure 1.1, we get

$$\int_{S_A} ((p - p_\infty)(\mathbf{i} \cdot \mathbf{n}) - (\boldsymbol{\tau_x} \cdot \mathbf{n})) \; dS = - \int_{S_F \cup S_D} (\rho (u - u_\infty)(\mathbf{q} \cdot \mathbf{n}) + (p - p_\infty)(\mathbf{i} \cdot \mathbf{n}) - (\boldsymbol{\tau_x} \cdot \mathbf{n})) \; dS$$

On the left-hand side, the near-field drag is present, while the far-field drag is defined on the right-hand side. In particular, if the lateral faces and the upstream plane are

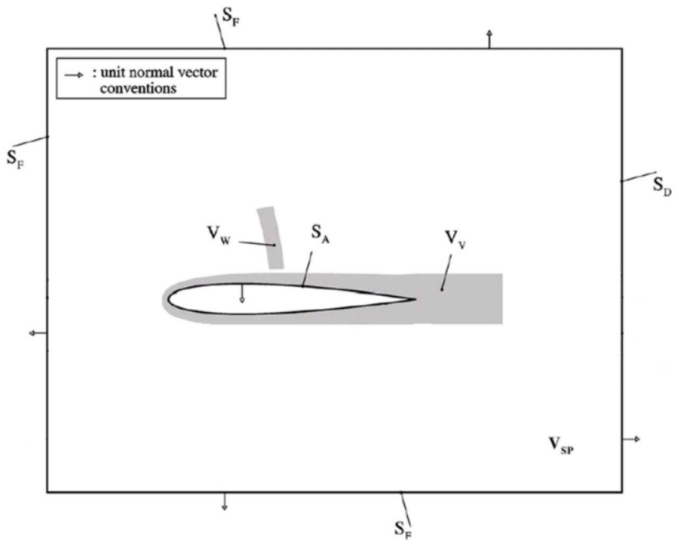

Figure 1.2: Definition of control volumes, boundaries and normal vectors in Van der Vooren and Desterac formulation [3].

sufficiently far from the source of drag, the integral can be extended only on the plane S_d.

The axial velocity can be expressed as a function of termodynamic variables [12]

$$u = u_\infty \sqrt{1 + \frac{2\Delta H}{u_\infty^2} - \frac{2}{(\gamma-1)M_\infty^2}\left(e^{\frac{\gamma-1}{\gamma}\frac{\Delta s}{R}}\left(\frac{p}{p_\infty}\right)^{\frac{\gamma-1}{\gamma}} - 1\right) - \frac{v^2+w^2}{u_\infty^2}} \tag{1.1}$$

where ΔH is the variation of stagnation enthalpy and Δs is the variation of entropy.

The Van der Vooren and Desterac idea is to break down the integral related to the far-field drag. If it is assumed that only the profile drag is exerted on the body, which means that the flow is free of vortices [12], the following assumptions can be made in the wake plane.

$$\boldsymbol{\tau_x} = 0 \qquad v = w = 0 \qquad p = p_\infty$$

Under these assumptions, the axial velocity defect can be expressed as

$$\Delta\bar{u} = u - u_\infty = u_\infty \sqrt{1 + \frac{2\Delta H}{u_\infty^2} - \frac{2}{(\gamma-1)M_\infty^2}\left(e^{\frac{\gamma-1}{\gamma}\frac{\Delta s}{R}} - 1\right)} - u_\infty$$

The authors define the profile drag as the total far-field drag

$$D = D_{vw} = -\int_{S_D} \rho\Delta\bar{u}(\mathbf{q}\cdot\mathbf{n})\, dS$$

With the definition of the shock and viscous domain, as in figure 1.2, and using the divergence theorem, the profile drag can be broken down into the contributions

$$D_w = -\int_{V_W} \nabla \cdot (\rho \Delta\bar{u}\mathbf{q})\, dV$$

$$D_v = -\int_{V_V} \nabla \cdot (\rho \Delta\bar{u}\mathbf{q})\, dV$$

The induced drag is finally defined by the authors as the complementary part, that is

$$D_i = -\int_{V_W \cup V_V} \nabla \cdot (\rho(u - u_\infty - \Delta\bar{u})\mathbf{q} + (p - p_\infty)\mathbf{i} - \boldsymbol{\tau_x})\, dV - D_p - D_f$$

where the property of the vector $\boldsymbol{f}$ has been used.

$$\nabla \cdot \boldsymbol{f} = \nabla \cdot (-\rho(u - u_\infty)\mathbf{q} - (p - p_\infty)\mathbf{i} + \boldsymbol{\tau}_x) = 0\,.$$

1.4 Unsteady formulations

Generalizing the far-field breakdown to unsteady flows is not as straightforward as it might seem. The first formulation for unsteady flows was proposed by Gariépy in 2013. In his formulation, he adds a term due to the unsteadiness of the flow and includes it in a new term, the unsteady drag D_{uns}.

However, the definition of this term is not related to any specific phenomenology. This is where Toubin's work begins, aiming to eliminate this term by accounting for the unsteadiness of the flow in each drag component.

1.4.1 Gariépy formulation

This formulation is written for a non-inertial reference frame [4]. In fact, Gariépy starts from the far-field equation.

$$\frac{\partial}{\partial t}\int_V \rho(u - u_\infty)\, dV + \int_{\partial V} (\rho(u - u_\infty)(\mathbf{q}_r \cdot \mathbf{n}) + (p - p_\infty)(\mathbf{i} \cdot \mathbf{n}) - (\boldsymbol{\tau}_x \cdot \mathbf{n}))\, dS + \int_V a_x\, dm = 0$$

where $\boldsymbol{q_r}$ denotes the relative velocity and a_x the relative acceleration in the x direction of the control volume.

Gariépy applies the same assumptions as Van der Vooren and Desterac to define the irreversible axial velocity defect $\Delta\bar{u}$, which, however, is undefined in certain regions of the domain, particularly in unsteady cases. This creates the need for a new expression for the axial velocity defect using the reversible axial velocity u_*.

$$\Delta\bar{u}_* = u - u_* = u_\infty \sqrt{1 + \frac{2\Delta H}{u_\infty^2} - \frac{2}{(\gamma - 1)M_\infty^2}\left(\left(\frac{p}{p_\infty}\right)^{\frac{\gamma-1}{\gamma}} - 1\right) - \frac{v^2 + w^2}{u_\infty^2}}$$

Analogous to the work of Van der Vooren, Gariépy divides the control volume into regions enclosing the source of drag and applies the divergence theorem to obtain

$$D_w = -\int_{V_w} \nabla \cdot (\rho \Delta \bar{u}_* \mathbf{q}_r)\ dV$$

$$D_v = -\int_{V_v} \nabla \cdot (\rho \Delta \bar{u}_* \mathbf{q}_r)\ dV$$

Gariépy also chooses to assign the neglected part to a new drag component, the spurious drag

$$D_{sp} = -\int_{V \setminus (V_w \cup V_v)} \nabla \cdot (\rho \Delta \bar{u}_* \mathbf{q}_r)\ dV$$

To define the component D_{uns}, he assumes that the variation of stagnation enthalpy is only due to reversible processes and linked to a time derivative. So, he defines a reversible axial velocity.

$$u_{*,s} = u_\infty \sqrt{1 - \frac{2}{(\gamma-1)M_\infty^2}\left(\left(\frac{p}{p_\infty}\right)^{\frac{\gamma-1}{\gamma}} - 1\right) - \frac{v^2+w^2}{u_\infty^2}}$$

He then defined the unsteady drag term with $u_{*,u} = u_* - {}_{*,s}$

$$D_{uns} = -\int_V \nabla \cdot (\rho u_{*,u} \mathbf{q}_r)\ dV - \frac{\partial}{\partial t}\int_V \rho(u - u_\infty)\, dV - \int_V a_x\, dm$$

and the induced drag component, defined as the complementary part in the total drag.

$$D_i = -\int_V \nabla \cdot (\rho u_{*,s} \mathbf{q}_r + (p - p_\infty)\mathbf{i} - \boldsymbol{\tau}_x)\ dV - D_p - D_f$$

Finally, the entire formulation can be summarized as

$$D_{nf} = D_p + D_f = D_w + D_v + D_i + D_{uns} + D_{sp}\,.$$

1.5 In-depth analysis of Toubin's formulation

Since this formulation is central to the work presented in this document, a section has been dedicated solely to this formulation to provide greater clarity.

Toubin begins by writing the mass and momentum balance in the control volume [12], obtaining

$$\int_V \frac{\partial \rho(\mathbf{q} - \mathbf{q}_\infty)}{\partial t}\,\mathrm{d}V = -\int_{\partial V} \rho(\mathbf{q} - \mathbf{q}_\infty)(\mathbf{q}\cdot\mathbf{n})\,\mathrm{d}S - \int_{\partial V}(p - p_\infty)\mathbf{n}\,\mathrm{d}S + \int_{\partial V}(\boldsymbol{\tau}\cdot\mathbf{n})\,\mathrm{d}S$$

The drag component is obtained by taking only the component parallel to the freestream velocity. By dividing the control volume boundary as in figure 1.1 and rearranging the terms, she obtains

$$\int_{S_a} ((p-p_\infty)(\mathbf{i}\cdot\mathbf{n}) - (\boldsymbol{\tau}_x\cdot\mathbf{n}))\,\mathrm{d}S = \int_{S_e} (-\rho(u-u_\infty)(\mathbf{q}\cdot\mathbf{n}) - (p-p_\infty)(\mathbf{i}\cdot\mathbf{n}) + (\boldsymbol{\tau}_x\cdot\mathbf{n}))\,\mathrm{d}S - \int_{S_a} \rho(u-u_\infty)(\mathbf{q}\cdot\mathbf{n})\,\mathrm{d}S - \int_V \frac{\partial\rho(u-u_\infty)}{\partial t}\,\mathrm{d}V$$

The term on the left-hand side is the definition of the near-field

$$D_{nf}(t) = \int_{S_a} ((p-p_\infty)(\mathbf{i}\cdot\mathbf{n}) - (\boldsymbol{\tau}_x\cdot\mathbf{n}))\,\mathrm{d}S$$

while the term on the right-hand side is the far-field drag, which, with the notation used by Van der Vooren, can be written as

$$D_{ff}(t) = \int_{S_e} (\mathbf{f}\cdot\mathbf{n})\,\mathrm{d}S - \int_{S_a} \rho(u-u_\infty)(\mathbf{q}\cdot\mathbf{n})\,\mathrm{d}S - \int_V \frac{\partial\rho(u-u_\infty)}{\partial t}\,\mathrm{d}V \tag{1.2}$$

The first surface term corresponds to the momentum flux through the outer surface and the forces applied on S_e, similar to the steady-state scenario. The second surface term reflects the change in longitudinal momentum caused by the body's motion. The volume term captures the time dependence and the temporal evolution of momentum.

From equation (1.2), we can write the property of the vector $\boldsymbol{f}$ in the unsteady case

$$\nabla\cdot\mathbf{f} = \frac{\partial\rho(u-u_\infty)}{\partial t} \tag{1.3}$$

Toubin also uses the thermodynamic expression for the axial velocity (1.1). It is then decomposed into an irreversible part and a reversible part.

Toubin defines the irreversible velocity as the axial velocity in a wake plane, placed sufficiently far to apply the condition of flow free of vortices, so

$$p = p_\infty \qquad\qquad v = w = 0$$

From equation (1.1) we obtain

$$u_{irr} = u_\infty\sqrt{1 + \frac{2\Delta H}{u_\infty^2} - \frac{2}{(\gamma-1)M_\infty^2}\left(e^{\frac{\gamma-1}{\gamma}\frac{\Delta s}{R}} - 1\right)} \tag{1.4}$$

It should be noted, however, that the irreversible axial velocity is undefined in regions where

$$p^\circ < p_\infty$$

Afterward, she introduces these assumptions into $\boldsymbol{f}$ to obtain

$$\boldsymbol{f_{irr}} = -\rho\,(u_{irr}-u_\infty)\,\mathbf{q} + \boldsymbol{\tau_x}$$

$$\boldsymbol{f_{rev}} = \boldsymbol{f} - \boldsymbol{f_{irr}} = -\rho\,(u-u_{irr})\,\mathbf{q} - (p-p_\infty)\,\mathbf{i}$$

The last assumption made is that the profile drag is due to the irreversible part of the vector $\boldsymbol{f}$, while the induced drag comes from the complementary part.

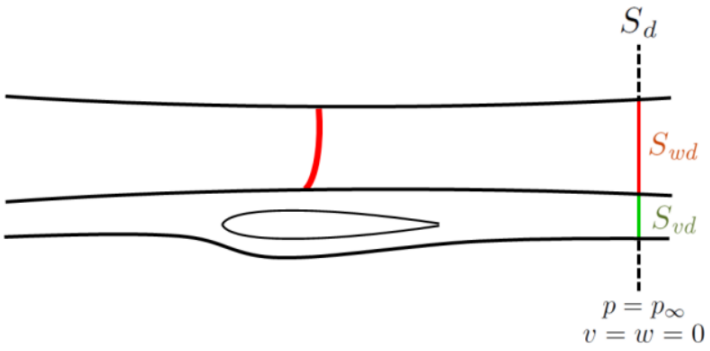

Figure 1.3: Definition of streamtubes for volume splitting. Image taken from [12].

1.5.1 Use of streamtubes like volume control

The drag breakdown is achieved by splitting the control volume into several smaller volumes, each containing a source of drag. In the following treatment, it is assumed that only one shock is present.

Toubin, in her treatment, creates the shock domain and the viscous domain using the concept of streamtubes, as shown in figure 1.3. This allows the integral on the wake plane to be transformed into an integral over the entire surface of the streamtube, since on the lateral faces the velocity is perpendicular to the normal, and on the upstream plane the irreversible velocity is equal to the freestream velocity.

1.5.2 Unsteady wave drag

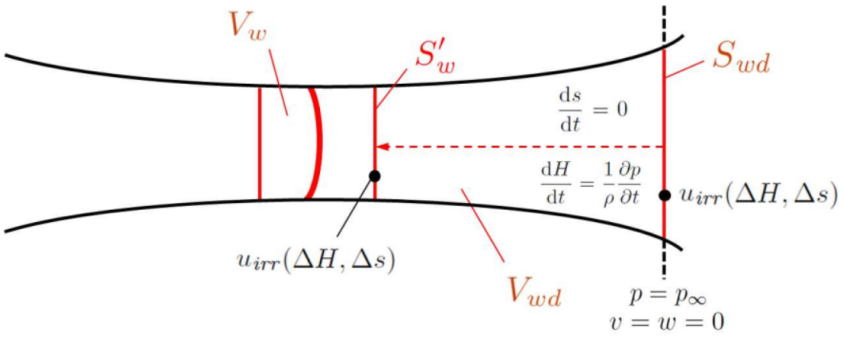

Figure 1.4: Definition of streamtubes for for shock volume. Image taken from [12].

Toubin analyzes the wave drag of an isolated normal shock moving in a perfect fluid [12]. As before, we focus on the streamtube enclosing the shock, that is $V_w \cup V_{wd}$, as shown

in figure 1.4. For the downstream boundary S_{wd}, we set the conditions such that

$$p = p_\infty \qquad\qquad v = w = 0$$

If the flow is supersonic, there is no information propagating upstream of the shock wave, so that the integration can be reduced to the downstream part of the streamtube. If we assume that the effect of $\boldsymbol{\tau_x}$ is negligible, the wave drag:

$$D = D_w = \int_{S_{wd}} -\rho\left(u_{irr} - u_\infty\right)(\mathbf{q}\cdot\mathbf{n})\,\mathrm{d}S - \int_{V_w \cup V_{wd}} \frac{\partial \rho(u-u_\infty)}{\partial t}\,\mathrm{d}V$$

Toubin attempts to move the downstream plane closer to the shock wave, so as to measure the entropy due solely to the shock. Using the divergence theorem and the mathematical relations valid in V_{wd}

$$\frac{Ds}{Dt} = 0 \qquad\qquad \frac{DH}{Dt} = \frac{1}{\rho}\frac{\partial p}{\partial t} + \nabla\cdot(\boldsymbol{\tau}\cdot\boldsymbol{q})$$

The unsteady wave drag [12] can be rewritten as

$$\begin{aligned} D_w = &\int_{S_w} -\rho\left(u_{irr} - u_\infty\right)(\mathbf{q}\cdot\mathbf{n})\,\mathrm{d}S - \int_{V_w} \frac{\partial \rho(u-u_\infty)}{\partial t}\,\mathrm{d}V \\ &- \int_{V_{wd}} \left(\frac{\partial \rho(u-u_{irr})}{\partial t} + \frac{1}{u_{irr}}\frac{\partial p}{\partial t}\right)\mathrm{d}V \end{aligned} \tag{1.5}$$

The first term is the momentum flux across the shock wave, and the second one is the rate of change in time. The last term accounts for the evolution of the entropy produced by the shock wave. The assumptions made to arrive at formulation (1.5) are two: the flow is isentropic in V_{wd} and the lateral face is a streamline, so that $\boldsymbol{q}\cdot\boldsymbol{n} = 0$.

1.5.3 Unsteady viscous drag

To create a formulation for the viscous drag, Toubin considers a profile isolated in a flow, without shock waves and reversible processes [12]. She works again with a streamtube that encloses the boundary layer and the wake. Neglecting the contribution from the upstream part, she obtains

$$D_v = \int_{S_v} \left(-\rho\left(u_{irr} - u_\infty\right)\mathbf{q} + \boldsymbol{\tau_x}\right)\cdot\mathbf{n}\,dS - \int_{V_v} \frac{\partial\left(\rho(u-u_\infty)\right)}{\partial t} dV \tag{1.6}$$

The distance from the body can be tuned, in order to reduce numerical errors.

1.5.4 Unsteady induced drag

The induced drag is defined by Toubin as the complementary part of the drag [12]. The complementary volume is defined as $V_c = V/(V_v \cup V_w \cup V_{wd})$ and the complementary downstream surface as $S_{cd} = S_d/(S_{vd} \cup S_{wd})$, as shown in figure 1.5.

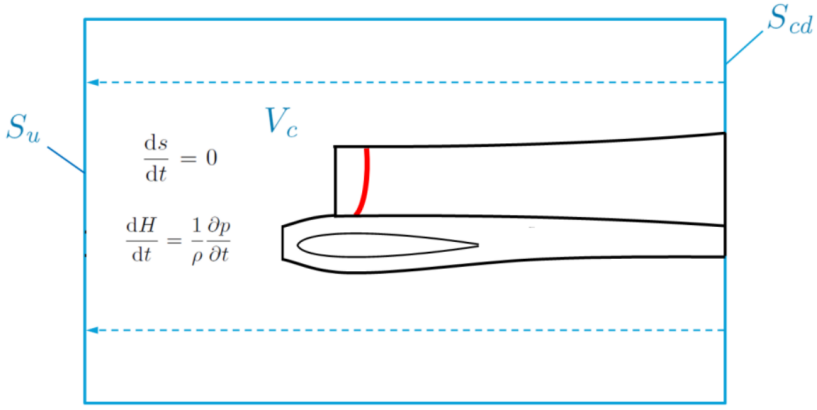

Figure 1.5: Complementary volumes and surfaces. Image taken from [12].

Toubin again neglects the contribution of the shear stress tensor for the irreversible part. The unsteady induced drag is

$$\begin{aligned} D_{ui} = &\int_{S_d} \left(-\rho\left(u - u_{irr}\right)\mathbf{q} - \left(p - p_\infty\right)\mathbf{i}\right) \cdot \mathbf{n}\, dS \\ &+ \int_{S_{cd}} -\rho\left(u_{irr} - u_\infty\right)\left(\mathbf{q} \cdot \mathbf{n}\right) dS - \int_{V_c} \frac{\partial}{\partial t}\left(\rho\left(u - u_\infty\right)\right) dV \end{aligned} \tag{1.7}$$

As done for the unsteady wave drag expression, the integral on S_{cd} can be moved into the volume integral and the downstream plane can be moved up to the upstream plane, thus obtaining

$$D_{ui} = \int_{S_e} \left(-\rho\left(u - u_{irr}\right)\mathbf{q} - \left(p - p_\infty\right)\mathbf{i}\right) \cdot \mathbf{n}\, dS - \int_{V_c} \left(\frac{\partial}{\partial t}\left(\rho\left(u - u_{irr}\right)\right) + \frac{1}{u_{irr}}\frac{\partial p}{\partial t}\right) dV$$

where S_e is the entire external surface of the domain.

In search of a further decomposition of the unsteady induced drag, Toubin isolates another term and links it to acoustic effects [12]. A further decomposition is then performed

$$D_{pa} = \int_{V_c} \frac{\rho(u_{irr} - u)}{a}\frac{\partial R^+}{\partial t} dV$$

$$D_i = \int_{S_e} \left(-\rho(u - u_{irr})\mathbf{q} - \left(p - p_\infty\right)\mathbf{i}\right) \cdot \mathbf{n}\, dS - \int_{V_c} \rho(u - u_{irr})\left(\frac{1}{a} + \frac{1}{u_{irr}}\right)\frac{\partial u}{\partial t} dV$$

where $R^+ = u + 2a/(\gamma - 1)$ is the Riemann invariant.

1.5.5 Final Toubin formulation

$$D_w = \int_{S_w} -\rho(u_{irr}-u_\infty)(\mathbf{q}\cdot\mathbf{n})\,dS - \int_{V_w} \frac{\partial \rho(u-u_\infty)}{\partial t}\,dV - \int_{V_{wd}} \left(\frac{\partial \rho(u-u_{irr})}{\partial t} + \frac{1}{u_{irr}}\frac{\partial p}{\partial t}\right) dV$$

$$D_v = \int_{S_v} (-\rho(u_{irr}-u_\infty)\mathbf{q} + \boldsymbol{\tau}_x)\cdot\mathbf{n}\,dS - \int_{V_v} \frac{\partial \rho(u-u_\infty)}{\partial t}\,dV$$

$$D_i = \int_{S_e} (-\rho(u-u_{irr})\mathbf{q} - (p-p_\infty)\mathbf{i})\cdot\mathbf{n}\,dS - \int_{V_c} \rho(u-u_{irr})\left(\frac{1}{a}-\frac{1}{u_{irr}}\right)\frac{\partial u}{\partial t}\,dV$$

$$D_{pa} = \int_{V_c} \frac{\rho(u_{irr}-u)}{a}\frac{\partial R^+}{\partial t}\,dV$$

$$D_m = \int_{S_a} -\rho(u-u_\infty)(\mathbf{q}\cdot\mathbf{n})\,dS$$

$$D_{ff} = D_w + D_v + D_i + D_{pa} + D_m$$

$$D_{sp} = D_{nf} - D_{ff}$$

1.5.6 Assumptions made for the formulation

Since the whole volume is here taken into account, the spurious drag should come from both the numerical errors and the assumptions made during the demonstration. There are four [12]

- The flow was assumed isentropic in the complementary volume and in the wake of the shock.
- The viscous contribution in the equation for the stagnation enthalpy variation was neglected in the complementary volume and in the wake of the shock.
- The assumption of domains defined by streamtubes results in a zero contribution from the lateral faces. However, the domains defined by sensors are not streamtubes, which leads to an intrinsic error in the formulation.
- The longitudinal viscous stress vector was neglected outside the viscous volume.

A spurious drag can thus be defined, due to the physics we are neglecting

$$D_{sp}^{phy} = -\int_{V_c\cup V_{wd}} \left(\rho\frac{\partial u_{irr}}{\partial \Delta s}\frac{d\Delta s}{dt} + \frac{\partial u_{irr}}{\partial \Delta H}\nabla\cdot(\tau\cdot\mathbf{q})\right) dV + \int_{S_e\setminus S_{vd}} (\tau_x\cdot\mathbf{n})dS - \\ - \int_{S_{lat}} \boldsymbol{f_{irr}}\cdot\boldsymbol{n}\,dS$$

1.6 Implemented formulation

To reduce the error inherent in Toubin's formulation, a different formulation is implemented for all cases in this study.The objective is to achieve a decomposition starting from equation (1.2). In fact, it represents a momentum balance in the direction parallel to the freestream flow and is an exact equation.

The idea is to create the same domains that Toubin uses in her study to calculate the viscous drag and the wave drag. From these, the induced drag is determined as the complementary component.

In this formulation, there in not anymore the acoustic drag of the unsteady induced drag D_{ui} in the (1.7). However, the expression for the acoustic drag was found with the assumption that there is no temporal change in entropy in the complementary volume. In theory this is a valid assumption, but in practice the definition of the viscous and wave domains is not perfect, and in the complementary volume $V_c = V \setminus (V_v \cup V_w \cup V_{wd})$ there may be unsteady phenomena with entropy creation.

The only assumption made, which distinguishes the formulation from the balance equation (1.2), is to assume that the flow is isentropic and the viscous effects are neglected in V_{wd}.

With reference to Figure 1.6, the following formulation is implemented for this study.

$$D_w = \int_{S_w} (-\rho(u_{irr} - u_\infty)\boldsymbol{q} + \boldsymbol{\tau}_x) \cdot \mathbf{n}\, dS - \int_{V_w} \frac{\partial \rho(u - u_\infty)}{\partial t}\, dV - \int_{V_{wd}} \left(\frac{\partial \rho(u - u_{irr})}{\partial t} + \frac{1}{u_{irr}} \frac{\partial p}{\partial t} \right) dV$$

$$D_v = \int_{S_v} (-\rho(u_{irr} - u_\infty)\boldsymbol{q} + \boldsymbol{\tau}_x) \cdot \mathbf{n}\, dS - \int_{V_v} \frac{\partial \rho(u - u_\infty)}{\partial t}\, dV$$

$$D_i = \int_{S_e} (-\rho(u - u_{irr})\boldsymbol{q} - (p - p_\infty)\mathbf{i}) \cdot \mathbf{n}\, dS + \int_{\partial(V_c \cup V_{wd})} (-\rho(u_{irr} - u_\infty)\boldsymbol{q} + \boldsymbol{\tau}_x) \cdot \mathbf{n}\, dS - \int_{V_c} \frac{\partial \rho(u - u_\infty)}{\partial t}\, dV$$

$$D_m = \int_{S_a} -\rho(u - u_\infty)(\boldsymbol{q} \cdot \mathbf{n})\, dS$$

$$D_{ff} = D_w + D_v + D_i + D_m$$

$$D_{sp} = D_{nf} - D_{ff}$$

The streamtube hypothesis is no longer required for the definition of domains to achieve a correct formulation. However, it remains important for accurate drag decomposition. Indeed, the closer the domain is to a streamtube, the more the surface integral approaches the sole contribution given by the wake plane, which is the fundamental assumption of the formulation.

In this case, the error we commit regarding the system's physics is

$$D_{sp}^{phy} = -\int_{V_{wd}} \left(\rho \frac{\partial u_{irr}}{\partial \Delta s} \frac{d\Delta s}{dt} + \frac{\partial u_{irr}}{\partial \Delta H} \nabla \cdot (\tau \cdot \mathbf{q}) \right) dV$$

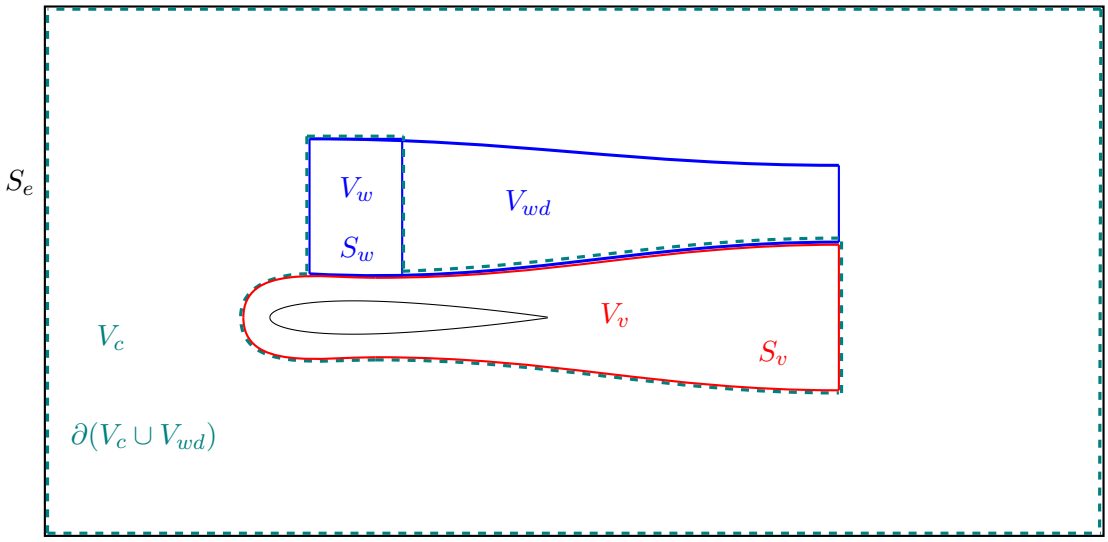

Figure 1.6: Definition of domains used in the implemented formulation. Downstream extension is parametric to have the most downstream surface of S_v and S_w in the wake's refinement region.

Chapter 2

Implementation in StarCCM+

The goal is to carry out the post-processing phase without using third-party software, without compromising accuracy. This approach eliminates the need for an external post-processor, accelerating the process and avoiding the storage of a large volume of data, which is particularly significant in unsteady three-dimensional simulations.

Various native solutions of StarCCM+ were studied, each with its pros and cons. The study focused on the accuracy of the integral calculations, particularly surface integrals.

Computational resources were provided by HPC@POLITO (`http://hpc.polito.it`).

2.1 Surface integral computation

Three methods were studied to calculate the surface integrals.

Isosurface The first method analyzed consists of computing the integral on an isosurface defined by the relative sensor. The sensor is a binary field function that is active when the cell belongs to a specific domain. The isosurface is set at a value of 0.5.

Although this method is easy to implement in both two-dimensional and three-dimensional cases, two main drawbacks arise.

The first is topological in nature and stems from the fact that the isosurface does not coincide with the cell faces. This leads to a discrepancy between the integration domain for the volume integral and that for the surface integral, as shown in figure 2.1. While this error is inevitable, it can be reduced if the cells are sufficiently small at the boundary of the integration domain.

The second error is numerical in nature. The software calculates the surface integral by projecting the cell-center value onto the isosurface. To reduce this error, one should avoid computing the surface integral in regions where there are high gradients of the quantities of interest. This error can be eliminated by using a first-order discretization scheme, albeit at the expense of solution accuracy.

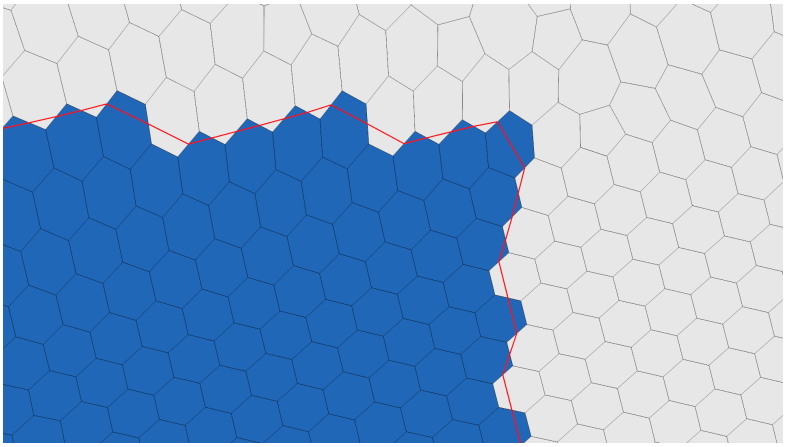

Figure 2.1: Isosurface to compute surface integrals. A discrepancy between the integration domains is evident. In this two-dimensional case, the red line denotes the isosurface, while the blue cells indicate the regions activated by the sensor.

Threshold It is a native function of the software, useful for defining an isolated group of cells through the use of the sensor. In this case, the error due to the integration surface is eliminated, as it now coincides with the cell faces.

However, even in this case the numerical error due to the integrand measured at the cell center persists. It is possible to compute the integral using node values, by employing an inverse distance weight method to interpolate the data stored at cell centers to vertices. The function at the cell node is calculated as

$$\varphi_v = \sum_i \frac{1}{d_i} \varphi_i$$

where φ_i is the value of the function at the cell centroid (to which the node belongs) and d_i is the distance from the cell center to the node.

Nevertheless, this interpolation yields mismatched results when a cell face coincides with an external face of the computational domain, where a boundary condition is applied.

Furthermore, this function can only be activated for three-dimensional cases. Therefore, another drawback is that in two-dimensional cases, mesh extrusion is required along with the solution of an additional momentum equation.

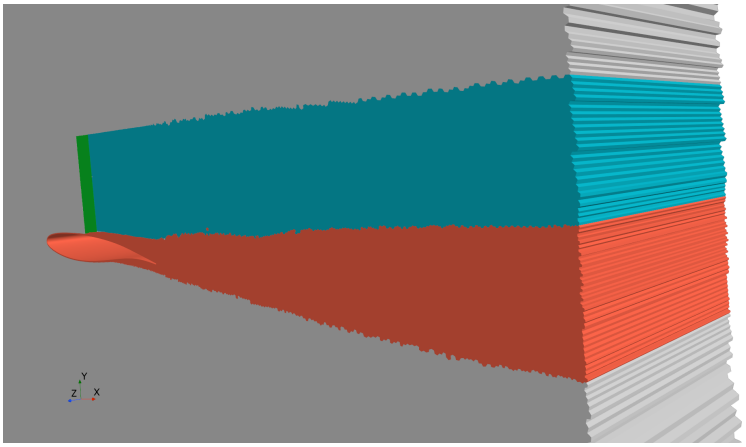

Figure 2.2: Cell groups defined via sensors. Note the mesh extrusion along the perpendicular direction.

Interface They are created by partitioning the computational domain based on sensors. Various subdomains are generated and connected through interfaces. None of the previously discussed errors is present. However, automating the creation of these interfaces is complicated, and the post-processing phase would become overly demanding, especially in highly unsteady cases where the domain changes shape over time.

2.2 Volume integral computation

A sensor δ_i is defined as a generic binary function that is active only in the regions of interest. In the case of using an isosurface, the volume integrals are calculated as

$$\int_V g\,\delta_i\,dV$$

However, if a group of cells V_i is defined for each domain using the native *threshold* function, the volume integral can be computed directly over that cell group, with the expression

$$\int_{V_i} g\,dV$$

The two results are equivalent. The choice between them depends solely on the method selected for the surface integral calculations.

2.3 Final model

For the reasons mentioned above, it was decided to use the domains defined by the thresholds, which in turn are based on the sensors. When referring to a two-dimensional

simulation, it will be understood that the computational domain consists of an extruded two-dimensional grid, with a cell one meter long. A symmetry condition is applied to each extruded face.

The computation of the surface integrals for the viscous and wave drags is performed on the surface of the threshold parts. Similarly, the surface integral of $\boldsymbol{f_{irr}}$ is computed for the induced drag. For the computation of $\boldsymbol{f_{rev}}$ for the induced drag, the entire computational domain has been considered, and the surface integrals are calculated along the domain boundaries.

The domain used for the two-dimensional cases is shown in Figure 2.3. The outlet of the domain has a downstream extension of 500 meters. The inlet, on the other hand, is composed of two splines, which form an angle of $\beta = 82.5$ degrees with the outlet. In the three-dimensional cases, the domain was generated by revolving it about the x-axis. The airfoil (or wing) studied in all cases has a chord length of $c = 1$ m.

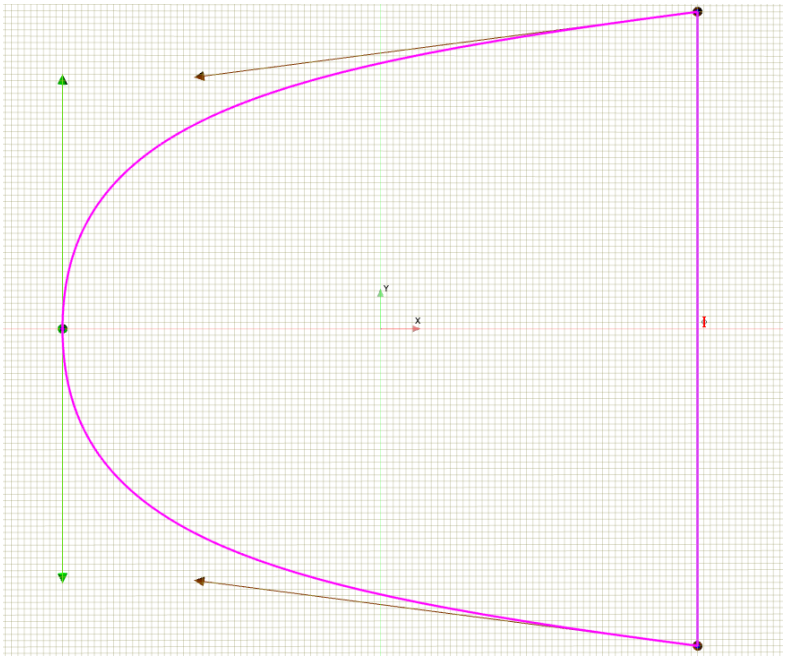

Figure 2.3: 2D sketch of the domain. Starting from the point with the highest y coordinate and proceeding in a counterclockwise direction, the coordinates in meters of the points are respectively (500,500), (-500,0), (500,-500).

The boundary condition for the inflow region is a stagnation inlet. The flow direction, total pressure, total temperature, and turbulent quantities are imposed. The total quantities are enforced using the isentropic relation.

The boundary condition applied to the outflow region is a pressure outlet. Pressure, temperature, and the freestream turbulent quantities are imposed.

The choice of the variable values to be applied at the domain boundaries is based on the Reynolds number and the Mach number at the fixed temperature $T_\infty = 300$ K.

The set air properties are the dynamic viscosity $\mu = 1.8550 \cdot 10^{-5}$ Pa $\cdot$ s, the molar mass $M = 29.966$ kg/kmol, and the specific heat at constant pressure $c_p = 1003.6$ J/(kg, K). The other quantities are then obtained as

$$V_\infty = Ma\,\sqrt{\gamma R T_\infty}$$

$$\rho_\infty = \frac{Re\,\mu}{V_\infty\,c}$$

$$p_\infty = \rho_\infty\,R\,T_\infty\,.$$

For the study of inviscid flows, $p_\infty = 101325$ Pa is set and the density is derived from the ideal gas law.

Given that $M_\infty < 1$ is always maintained and the temperature field is limited, no variational law was applied for the dynamic viscosity and the specific heat at constant pressure, which therefore remain constant throughout the domain.

Regarding the temporal derivatives, a second-order accurate backward discretization is used. In particular, the last three solutions of the quantities to be differentiated are temporarily stored, and the temporal derivative in cell n at time step k is computed as

$$\left(\frac{\partial \varphi}{\partial t}\right)_n^k = \frac{\varphi_n^{k-2} - 4\,\varphi_n^{k-1} + 3\,\varphi_n^k}{2\,\Delta t}\,.$$

All post-processing for the drag decomposition is performed at each time step.

2.3.1 Sensors for the definition of domains

Various sensors have been tested for decomposing the different sources of drag, with particular attention given to those described by Toubin [12].

Several sensors for detecting the shock wave are available in the literature. The one used for these studies is the one defined by Toubin

$$\delta_w = 1 \iff \begin{cases} \boldsymbol{v} \cdot \nabla p \geq k_{w1}\,a\,|\nabla p| \\ |\nabla p| > k_{w2} \end{cases} \tag{2.1}$$

where k_{w1} has a value slightly below unity.

Regarding the definition of the viscous domain, there is a generation of entropy and vorticity due to the dissipative effects at the wall. These two quantities are subsequently transported along the wake by the convective flow. The sensor definition is therefore

$$\delta_v = 1 \iff \begin{cases} \Delta s > k_{s,v}\,s_\infty \\ ||\boldsymbol{\Omega}|| > k_{\omega,v} \\ \delta_w = 0 \end{cases} \tag{2.2}$$

The viscous sensor described above has a general validity, but care must be taken not to consider cells that are activated due to numerical errors. A more accurate sensor can

be adopted for turbulent flows. It is based on the turbulent viscosity ratio $\mu_r = \mu_t/\mu$ and the strain rate tensor $\boldsymbol{S}$ and it's defined as

$$\delta_v = 1 \iff \begin{cases} \mu_r > 1 \\ ||\boldsymbol{S}|| > k_\tau \, \overline{\tau_w} \\ \delta_w = 0 \end{cases} \tag{2.3}$$

where $\overline{\tau_w}$ is the average skin friction at the wall and $k_\tau = 0.1$ is a coefficient. In both viscous sensors, the prism layers cells are added to ensure that u_{irr} is defined on the boundary of the viscous domain.

Across the shock wave, there is an increase in entropy that is subsequently transported by convective phenomena along the wake. Moreover, a low vorticity value is present downstream of the shock. The sensor for the shock wake can be expressed as

$$\delta_{wd} = 1 \iff \begin{cases} \Delta s > k_{s,w} \, s_\infty \\ ||\boldsymbol{\Omega}|| < k_{\omega,w} \\ \delta_w = 0 \\ \delta_v = 0 \end{cases} \tag{2.4}$$

Chapter 3

Steady cases with unsteady methods

Several steady cases have been studied to evaluate the far-field decomposition and the study of the domains, particularly their downstream extension. A steady solution is first found until convergence is reached, and then an unsteady simulation is performed to validate the implemented model.

These cases are important to evaluate the individual drag contributions and their interaction, as well as to compare them with values found in the literature.

3.1 Assessment of viscous drag

The study cases are related to a two-dimensional turbulent flow over a NACA0012 airfoil with angle of attack $\alpha = 0°$. The Tognaccini case [10] was carried out with $M_\infty = 0.7$ and $Re = 9 \cdot 10^9$. We use them to evaluate the viscous drag and induced drag for the zero incidence case. All the drag coefficients are presented as drag count. All cases were simulated using a second-order accurate discretization scheme and Roe's flux scheme.

Four different meshes were used. Three of these are structured and are specifically designed for the NACA0012 at zero incidence [8], while the other is an unstructured mesh with polygonal cells.

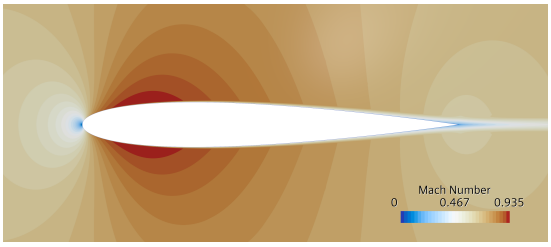

Figure 3.1: Mach number field.

Figure 3.2: Viscous domain definition.

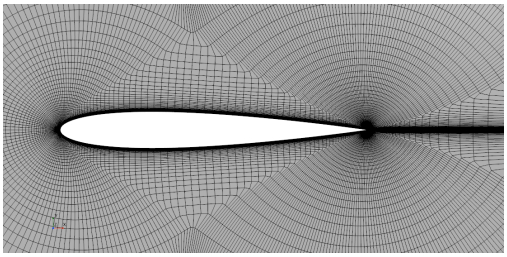

Figure 3.3: Grid with 449x129 resolution (57344 cells)

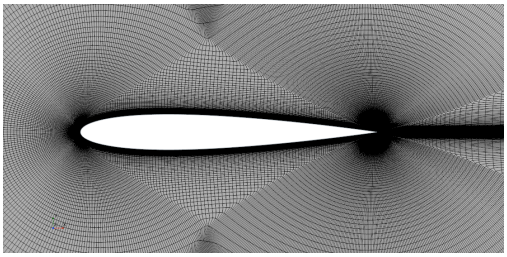

Figure 3.4: Grid with 897x257 resolution (229376 cells)

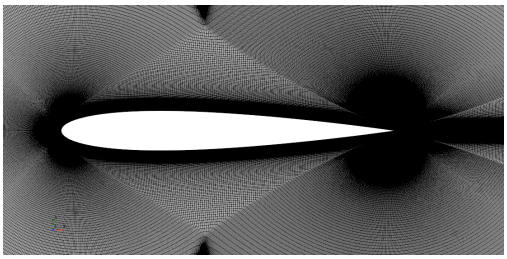

Figure 3.5: Grid with 1793x513 resolution (917504 cells)

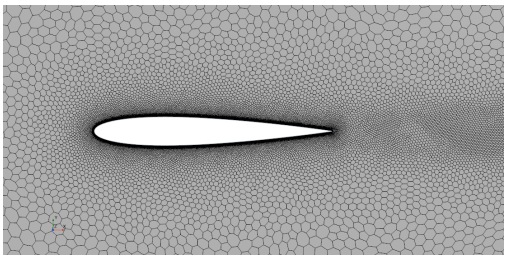

Figure 3.6: Polyhedral mesh (199350 cells) with sensor based refinement.

3.1.1 Results

The results are all presented in Table 3.1 and Figure 3.7. Excluding the coarsest mesh from this discussion, the far-field drag coefficient is very close to the near-field one.

For the structured meshes, the error increases the further away from the body you get. This could be due to the high aspect ratio of the cells in areas further from the profile. The behavior of the unstructured mesh is different, where a minimum is present between 10 and 12 chord lengths from the trailing edge.

Overall, differences remain small, on the order of a few drag counts—and are similar across structured and unstructured grids, though unstructured meshes may show slightly larger oscillations. So, extending the domain to 10 chord lengths seems to be sufficient to achieve accurate far-field drag estimates.

In the drag decomposition, there is also a small component of induced drag. Although this component is small, it should be zero. Its presence can be associated with a definition of the viscous domain that does not cover all the irreversible phenomena present, which are accounted for in the complementary volume $V_c = V \backslash V_v$.

Table 3.1: Results compared to Tognaccini studies [10]. All values were taken at a downstream extension of 10 chord lengths.

	C_L	C_D	CD_{ff}	CD_w	CD_v	C_{D_i}
Tognaccini	0	79	78.6	0	78.6	0
Nasa (coarse)	0	77.1	77.5	0	78.3	-0.72
Nasa (medium)	0	78.5	78.8	0	78.8	-0.05
Nasa (fine)	0	79.1	79.2	0	79.1	0.14
Unstructured	0	75.8	76.3	0	76.0	0.31

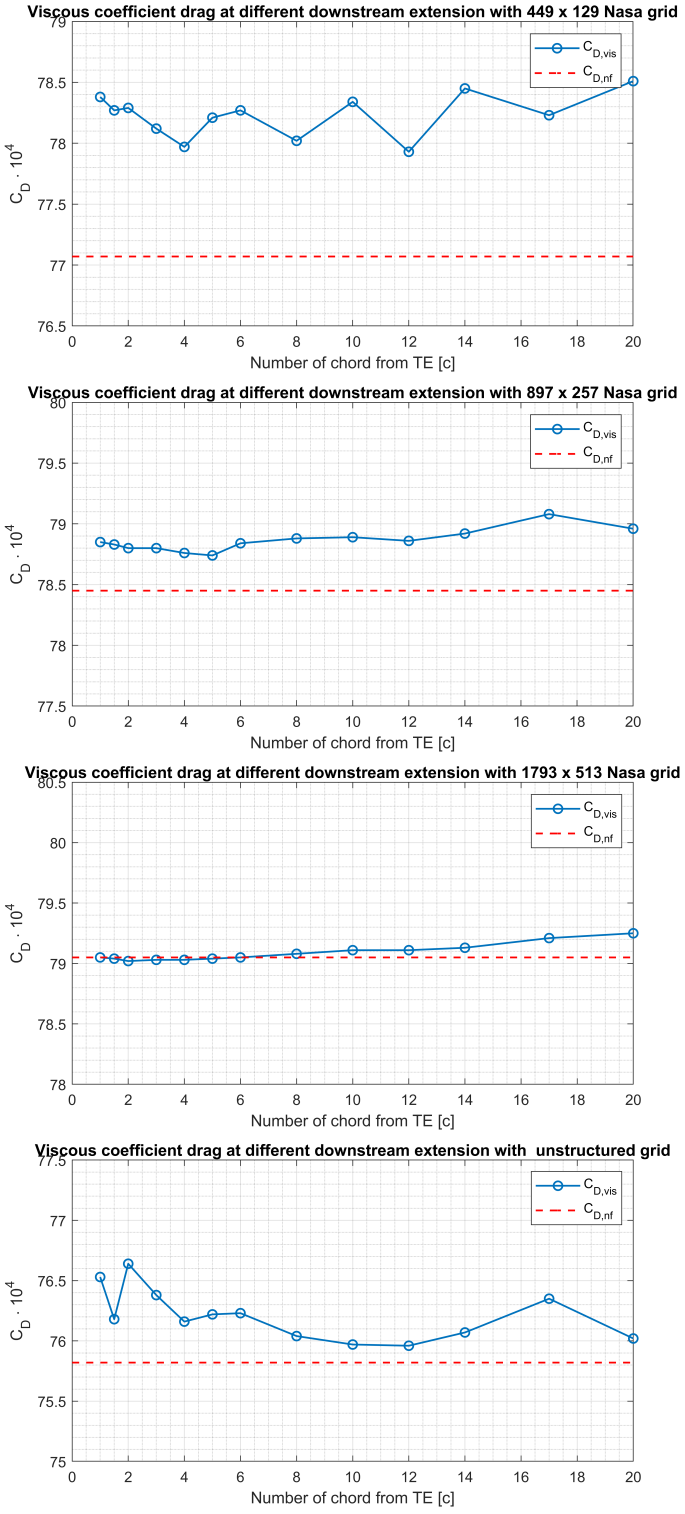

Figure 3.7: Far field drag coefficient with different downstream extension

3.2 Assessment of wave drag

In order to predict the accuracy of the wave drag calculation, a two-dimensional simulation with an inviscid and transonic flow was carried out. The objective is to study the effectiveness of the wave sensor. For this reason, a comparison is made between the sensor and a box in which the sensor is contained.

The airfoil is a NACA-0012 placed at an incidence of $\alpha = 2°$ and is exposed to a flow with a Mach number of $M = 0.8$. The discretization scheme is second-order accurate, and the advection upstream splitting method (AUSM) is used for the flux calculation at the interface. In figure 3.8, the Mach number field near the airfoil is shown.

The computational grid consists of 170590 polyhedral cells. An adaptive refinement is applied in the region where the shock wave is present. A coarser refinement is also performed in the vicinity of the shock, where the integration box is located. The mesh is depicted in Figure 3.9. The imposed refinement allows the inviscid shock wave to be resolved and captured in 2 cells.

3.2.1 Results

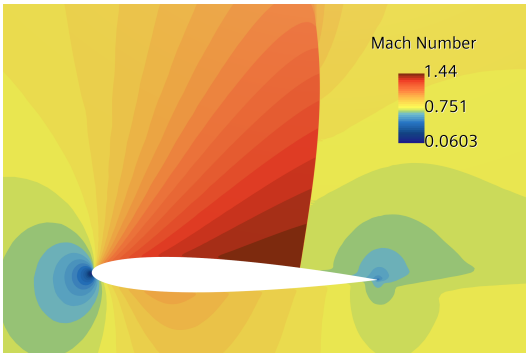

Figure 3.8: Mach number field.

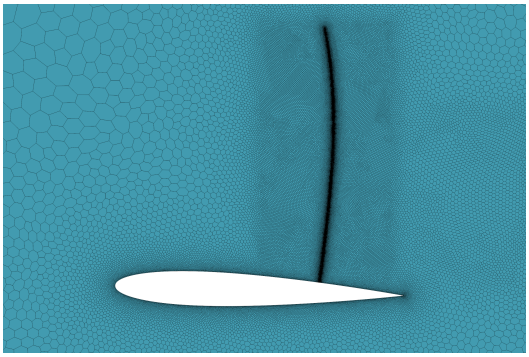

Figure 3.9: Computational grid.

From the solution, the minimum and maximum coordinates of the shock sensor were extracted for each Cartesian axis. Using these values, a box was created that encloses the drag source, although it is somewhat removed from the strong gradients present at the shock. Moreover, along the axis parallel to the freestream velocity vector, the box can be extended to study its effects on the drag decomposition. In Figure 3.10, the boxes described above are shown.

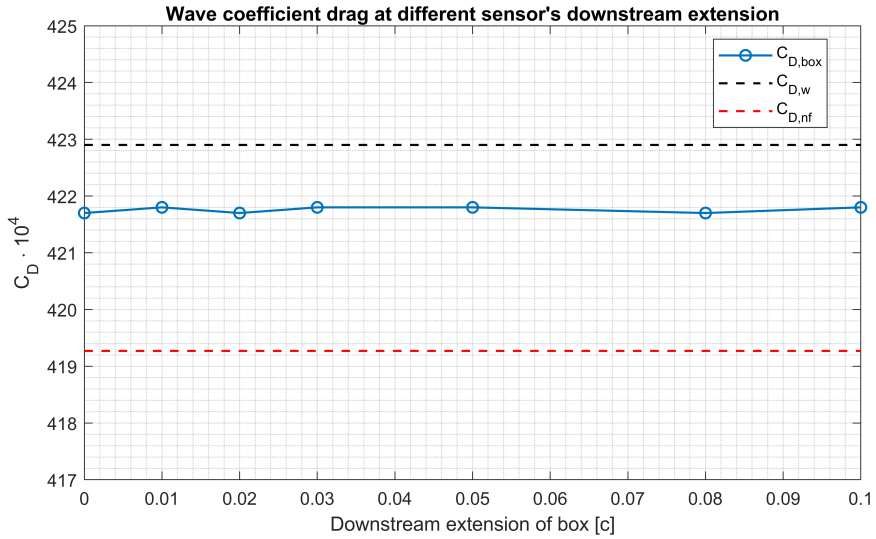

Figure 3.11: Wave drag computation in the volume control defined by the box.

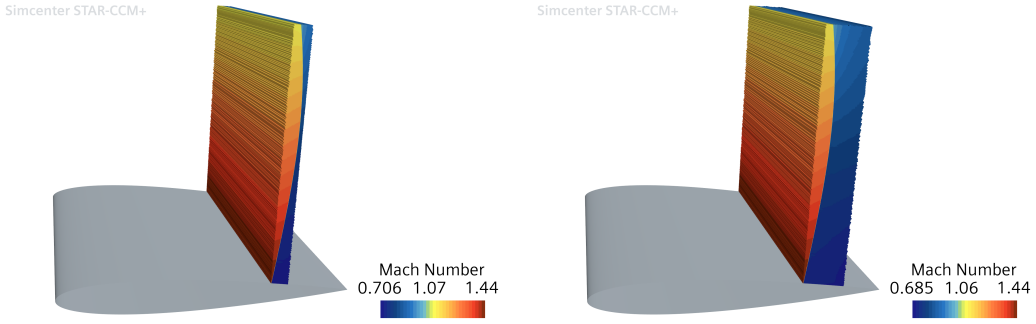

Figure 3.10: Box in which the shock wave is enclosed. The downstream extension is variable and can be adjusted by the user via a parameter.

Various values of downstream extension are compared to analyze the obtained wave drag, along with that relative to the volume defined solely by the shock sensor. In Figure 3.11, the trend of the wave drag is presented as a function of the box's downstream extension, expressed in chord lengths.

What is observed is that the integration method is not affected by the downstream extension of the box that encloses the shock. The trend is practically constant and is within one drag count of the wave drag value calculated with the surface integral over the viscous domain defined by (2.1).

After this study, it was decided to adopt the box that encloses the shock rather than the shock sensor itself, in order to achieve a more accurate solution. No further extension of the downstream face of the new volume is applied, as it does not affect the final result.

3.3 Interaction between viscous and wave drag

In their studies, Tognaccini et al. performed a drag decomposition on a NACA0012 airfoil in transonic flow and shared the results only graphically, as shown in Figure 3.12. The Tognaccini case [10] was conducted with $M_\infty = 0.7$ and $Re = 9 \cdot 10^6$. The discretization scheme is second-order accurate, and Roe's scheme and k-ω SST turbulence model are used. We use these results to evaluate the viscous drag and wave drag. All drag coefficients are presented in drag counts.

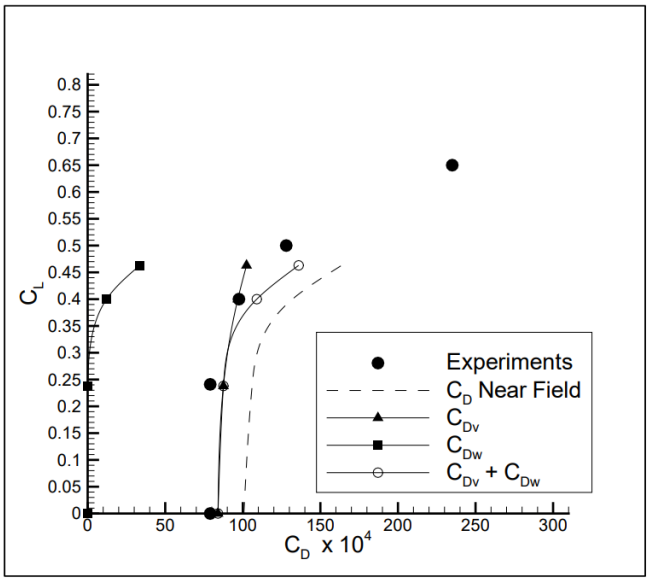

Figure 3.12: Drag decomposition in a transonic flow over a Naca0012 airfoil, with a Mach numebr $M = 0.7$ and a Reynolds number $Re = 9 \cdot 10^6$. [10]

To estimate the angle of attack of the airfoil, the studies by C. D. Harris [5] are useful. Several wind tunnel studies were conducted on a NACA0012 airfoil at different Mach numbers and Reynolds numbers. To assess the angle of attack, figure 3.13 is used, showing the normal force coefficient C_N as a function of the angle of attack. Since the angles of incidence are small, the following assumption is made:

$$C_N = C_L * cos(\alpha) \sim C_L \, .$$

By interpolating the data using pixel analysis of both images, an incidence angle of $\alpha = 2.73°$ is obtained. The interpolated results are presented in the table 3.2.

The computational grid consists of 188,726 polyhedral cells. Two local refinements were adopted, based on the sensors. A finer refinement was performed near the shock, while a coarser refinement was applied near the airfoil wall and along the wake, as shown in figure 3.15.

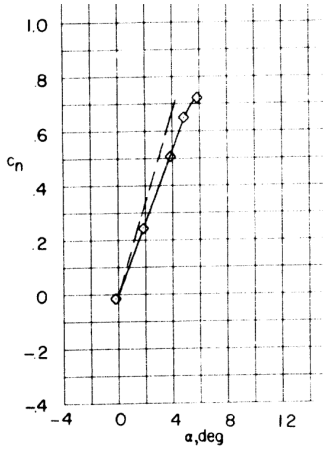

Figure 3.13: Normal force coefficient of NACA0012 airfoil with $M = 0.7$ and $Re = 9 \cdot 10^6$. Dash line indicates angle of attack correction for wall interfence. [5]

3.3.1 Results

The values of the drag decomposition and the comparison with the results found by Tognaccini et al. are shown in table 3.2. Although the lift coefficient matches the one obtained in [10], there is a slight discrepancy regarding the drag coefficient. This deviation is relatively small, and it is reasonable to assume that the percentage of decomposed drag components remains similar for these small variations. Therefore, in figure 3.17, the values of viscous drag and wave drag are compared to the total drag.

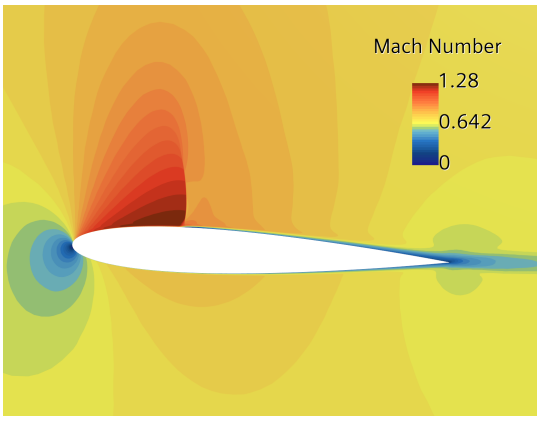

Figure 3.14: Mach number field.

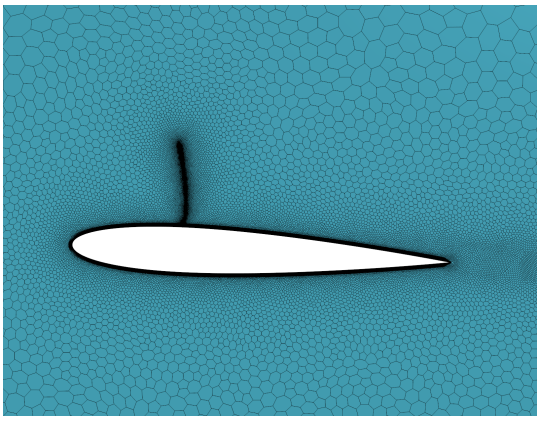

Figure 3.15: Computational grid.

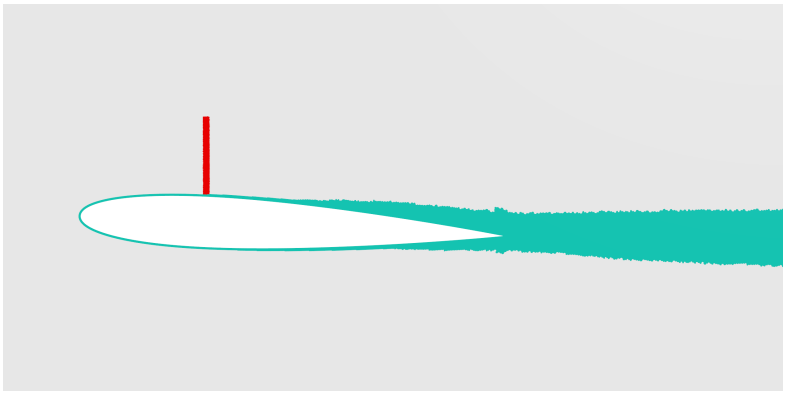

Figure 3.16: Viscous and wave domains, defined by sensors (2.3) and (2.1).

Given the reproducibility challenges encountered in the studies, the results can be considered reliable and fully comparable to the literature. When discussing percentages relative to total drag, the results differ by less than 2%.

Another potential discrepancy may arise. When the shock occurs in a viscous flow, an interaction between the shock and the boundary layer forms what is known as a lambda shock, depicted in figures 3.18 and 3.19. This small interaction region is included in the wave domain in this study, as it exhibits characteristics associated with shock waves, such as strong gradients and regions where the fluid remains supersonic. However, no mention of this interaction is found in Tognaccini's studies.

Table 3.2: Results compared to Tognaccini studies [10].

	C_L	C_D	CD_{ff}	CD_w	CD_v	C_{D_i}
Tognaccini	0.46	137	136	34	102	0
This study	0.462	127	127	29.6	97.7	-0.85

	$\frac{C_{D_w}}{C_D}$	$\frac{C_{D_v}}{C_D}$	$\frac{C_{D_i}}{C_D}$	$\frac{C_{D_{ff}}}{C_D}$
Tognaccini	0.248	0.752	0	0.993
This study	0.233	0.770	-0.00670	0.999

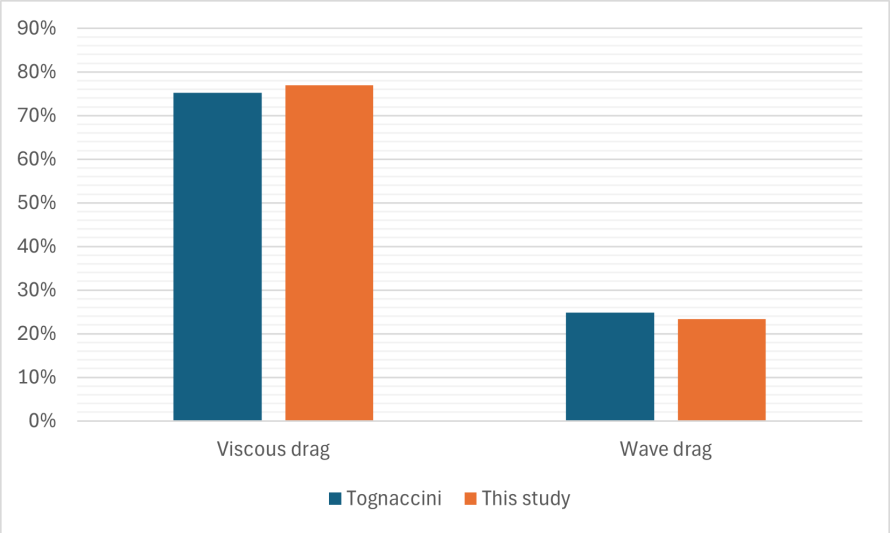

Figure 3.17: Viscous and wave drag values normalized by the total drag value.

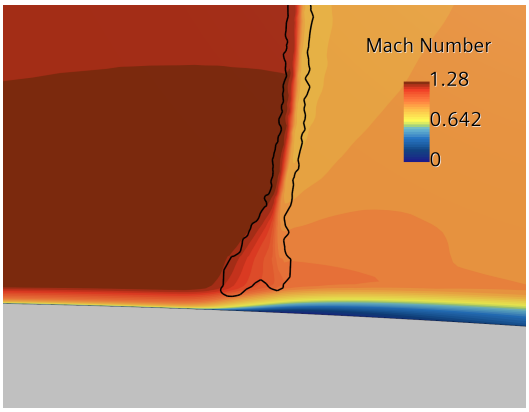

Figure 3.18: Detail of wave sensor near the lambda region.

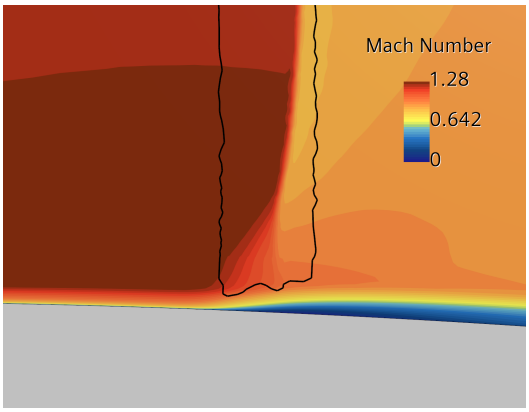

Figure 3.19: Detail of box enclosing the lambda shock wave.

3.4 Interaction between viscous, wave and induced drag

A three-dimensional case is analyzed in which all drag sources are present. The study is conducted on a rectangular planform wing, with a transonic flow at $M = 0.8$, $Re = 2.7 \cdot 10^6$, and an angle of attack $\alpha = 2.5°$. The wing section is a NACA0012 airfoil with a unit chord c, extruded to a length of $b/2 = 4, c$. The domain is generated exploiting the case symmetry, and a symmetry boundary condition is applied on the symmetry plane. The discretization scheme is second-order accurate, and the AUSM scheme and k-ω SST turbulence model are used

This is an interesting case to compare with the decomposition results obtained in the studies by Toubin [12] and Raffa [11].

The mesh is created using the trimmed mesher and consists of over 20 million cells. An adaptive refinement was employed using the same criteria as in the previous cases. The only difference is in the extension of the refinement along the wake, which stops at five chords downstream from the wing's trailing edge. Two snapshots of the mesh configuration are shown in figure 3.20.

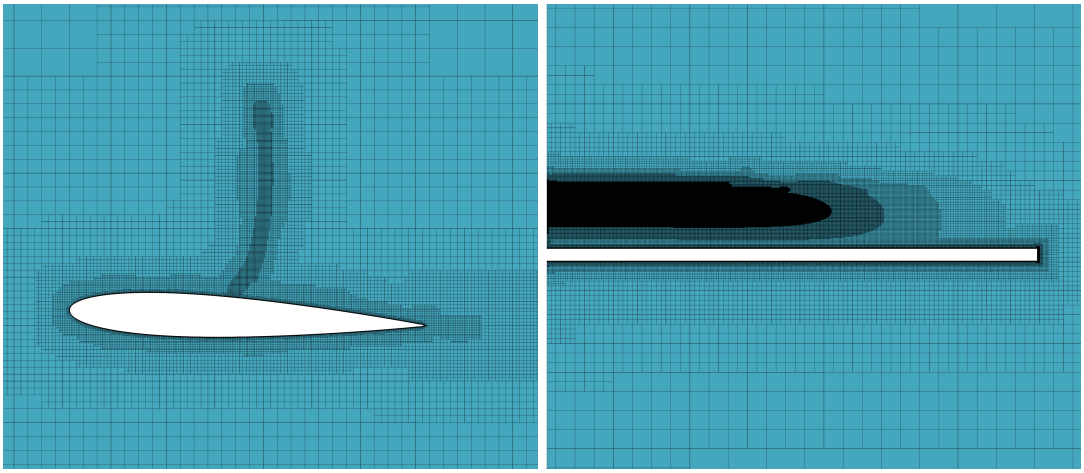

Figure 3.20: Mesh adopted in the three-dimensional case. The symmetry plane and the cross-section perpendicular to the freestream flow, positioned at a distance $x_1 = 0.41\,c$ from the leading edge, are depicted.

3.4.1 Results

A preliminary steady simulation was carried out. Once convergence was reached, the steady solver was activated. In figure 3.21, the Mach number is shown on a plane whose normal is parallel to the freestream direction and positioned at a distance $x_0 = 0.5\,c$ from the wing's trailing edge. The streamlines highlight the effect of the wingtip vortices, colored with the pressure coefficient.

In figure 3.22, the three domains based on the sensors (2.3), (2.1) and (2.4) are displayed. An additional domain was included for completeness, but its presence is

practically inconsequential to the final result, contributing less than 0.1%.

Table 3.3 presents the results of the decomposition, compared with those of Toubin and Raffa. The results are very close, although not exactly identical. However, the best correlation between near-field drag and far-field drag observed in this study indicates that the method and its implementation are working well. It is important to pay attention to the definition of the domains, as this is the only element that seems to make a real difference in the decomposition values and cannot be directly compared with the studies by Toubin and Raffa.

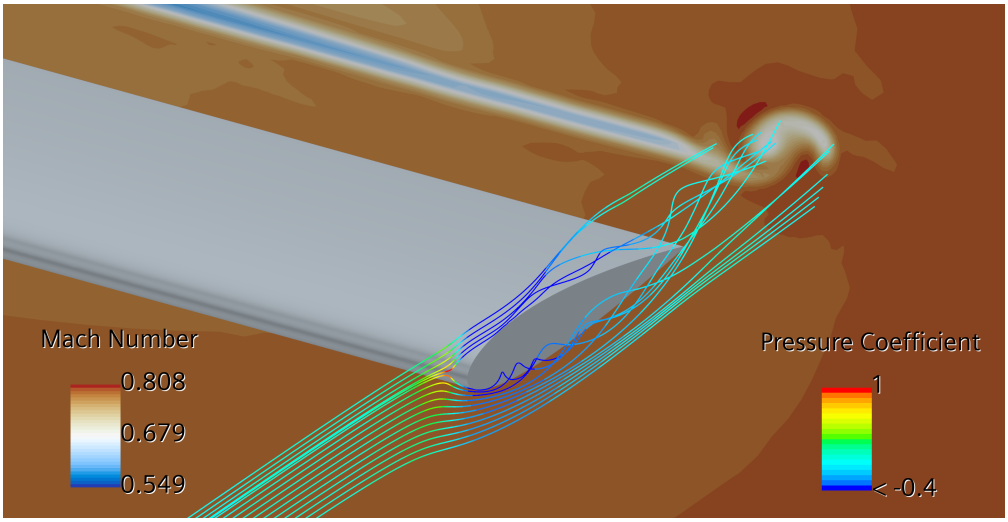

Figure 3.21: Mach number field in a downstream plane respect to wing. Streamline are shcwn to enhance the tip vortex effect.

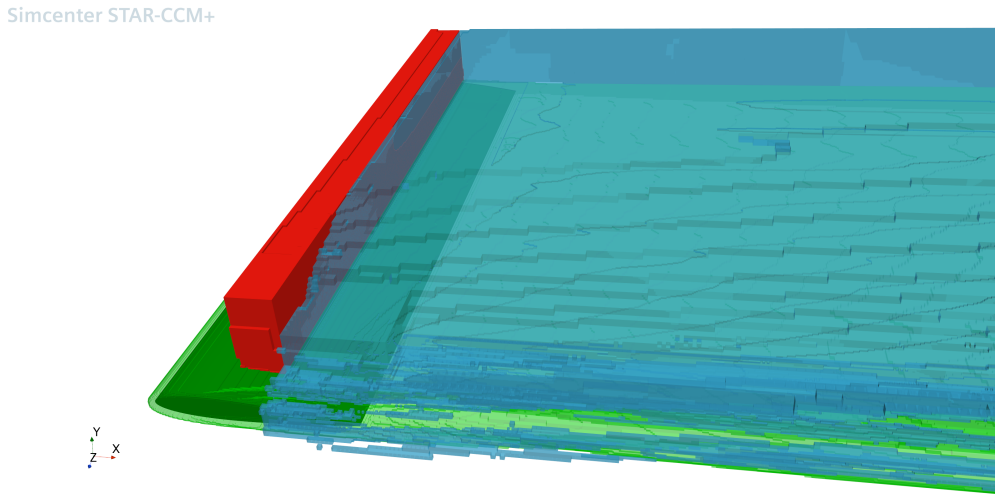

Figure 3.22: Definition of domain in the three-dimensional case.

Table 3.3: Results compared to Toubin and Raffa studies.

	C_D	CD_{ff}	CD_w	CD_v	C_{D_i}
Toubin	283	285	154	104	27.0
Raffa [11]	279.0	280.85	165	92	27
This study	281.4	281.6	162.3	89.23	30.04

In this simulation, the definition field of the axial irreversible velocity u_{irr} can also be appreciated. In fact, it is not defined in regions where the following relation holds

$$p^{\circ} < p_{\infty} \, .$$

The total pressure is an indicator of the energy possessed by the fluid element, in terms of both static and dynamic pressure. In this case, u_{irr} is not defined in regions very close to the wall and in the tip vortex area. The former is not problematic since the prism layer cells are automatically added to the viscous domain to enhance the robustness of the method. Particular attention must be given to the wingtip region. Here, to ensure that u_{irr} is always defined on the surface of the viscous domain, it was decided to assign not only the prism layers but all cells within a certain distance from the wing. In figure 3.23, the zones where the axial irreversible velocity is not analytically defined are highlighted.

The imbalance between viscous and wave drag compared to the case analyzed by Toubin may be due to the definition of wave volume. The position of the shock wave along the chord changes along the span, and the box enclosing the shock wave occupies a larger region of the viscous domain.

The comparison of the results with the analyzed data is satisfactory, considering the difference in the turbulence model, numerical scheme and mesh. In particular, Toubin uses the Spalart-Allmaras turbulence model and Jameson's scheme.

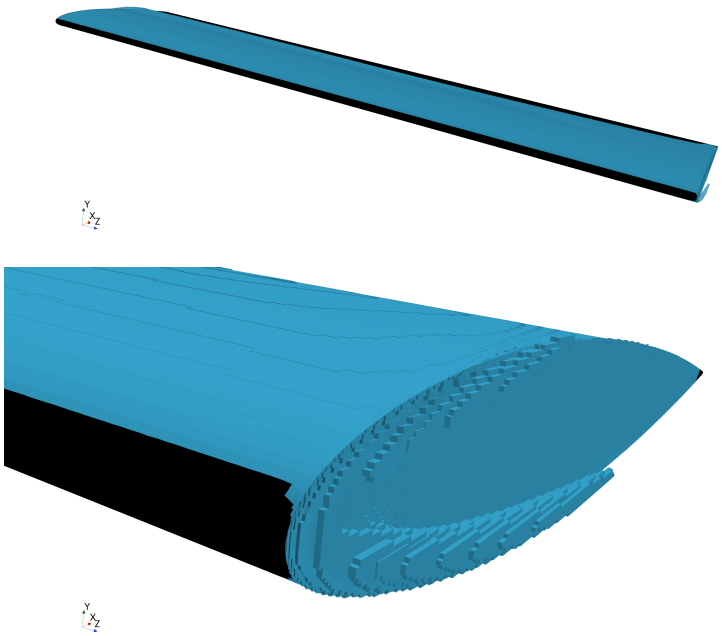

Figure 3.23: Regions of no definition of u_{irr}.

Chapter 4

Unsteady cases

Previous steady simulations have allowed us to better understand how to set up the various parameters for the model implementation. It is useful to summarize the results found in the previous chapter. In particular:

1. The extension of the viscous domain must include a sufficient portion of the wake to capture all irreversible phenomena, yet it should not be too distant from the body to avoid loss of accuracy in regions where low-quality cells are present. A compromise was found with an extension of 10 chords from the trailing edge.

2. The definition of the wave domain using the sensor (2.1) is a good choice. However, a slight gain in accuracy is possible by using the box that encloses the shock.

3. No study was conducted on V_{wd} since its contribution is negligible in steady cases.

4. Usually, the regions where the axial irreversible velocity is not defined are located near the wall. If these are not included in the prism layer cells, an appropriate tuning of the distance from the wall can ensure their inclusion in the viscous domain.

It is worth noting that the cases considered here involve phenomena that are relatively simple to capture with a fluid dynamics simulation. Therefore, the methodology applied in these cases might not be suitable for unsteady scenarios, where structures of different sizes form and interact with each other.

The computational grid for unsteady cases must be chosen appropriately to capture the phenomena of interest at every time instant. In all the simulations described in this chapter, the URANS equations are solved and a periodic pattern is observed in every case. For this reason, a local mesh refinement was performed after several periods of simulation to improve efficiency and reduce computational cost. However, an adaptive mesh refinement is required if LES simulations are to be performed, which are not addressed in this study.

4.1 Wake instability in a laminar flow

The first unsteady case concerns the unsteady instability formed in the wake of a two-dimensional profile in low Reynodls number flow. The airfoil is a NACA0012 with an angle of attack $\alpha = 6°$ to the freestream direction, with $M = 0.2$ and $Re = 5000$. The numerical scheme is a third order of accuracy and it use Roe's scheme to compute the flux at the interfaces.

Several periods were analyzed over time, and the results shown refer to the last period calculated. The vortex shedding develops periodically, with a period $T = 9.6 \cdot 10^{-3}$ s. The time step used is $\Delta t = 5 \cdot 10^{-5}$ s.

During the first 20 periods, the viscous sensor was monitored, and all cells in which the viscous sensor was activated at least once were recorded. Based on this history of the viscous domain, a mesh refinement was performed on the domain to improve the efficiency of the solution in terms of computational resources. A polyhedral mesh was used, with 118565 cells, as shown in figure 4.1.

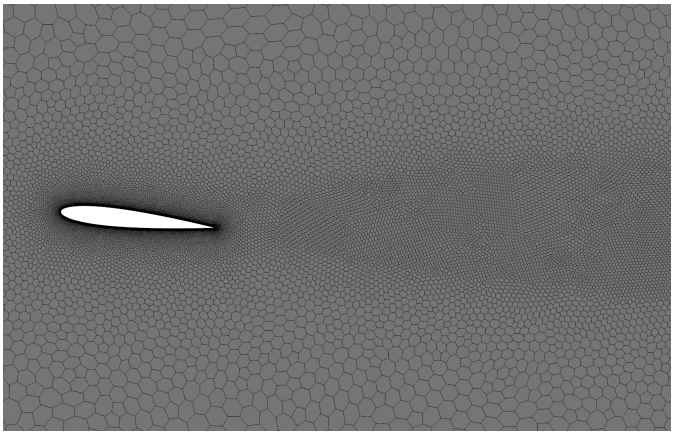

Figure 4.1: Mesh of laminar vortex shedding case.

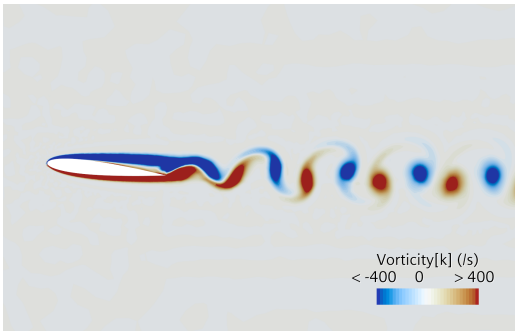

Figure 4.2: Z-component of vorticity.

Figure 4.3: Viscous domain definition.

4.2 Results

Several periods were completed before analyzing the drag decomposition. As shown in figure 4.11, the vortex due to wake instability is periodic and is subsequently transported by convective phenomena. The total drag coefficient reaches almost 710 drag counts as a maximum and 810 drag counts as a minimum.

The regions where u_{irr} is not defined are located near the airfoil, as shown in Figure 4.4. These regions have always been enclosed within the viscous domain.

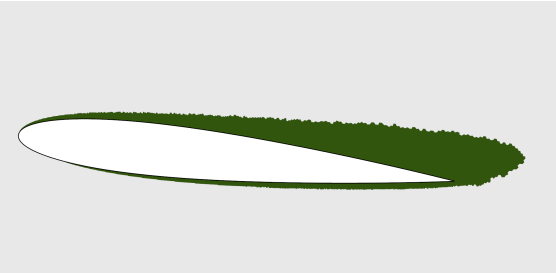

Figure 4.4: Regions where u_{irr} is not defined.

In addition to the viscous sensor defined by condition (2.2) the drag decomposition was also applied using a new sensor. Essentially, the viscous sensor is recorded at every time step throughout the entire period. Then, every cell that has been activated at least once by the viscous domain remains active for every subsequent time step k. Therefore

$$\delta_v^* = 1 \qquad \Longleftrightarrow \qquad \sum_{k=1}^{T/\Delta t} \delta_v^k \geq 1$$

The result is shown in Figure 4.5.

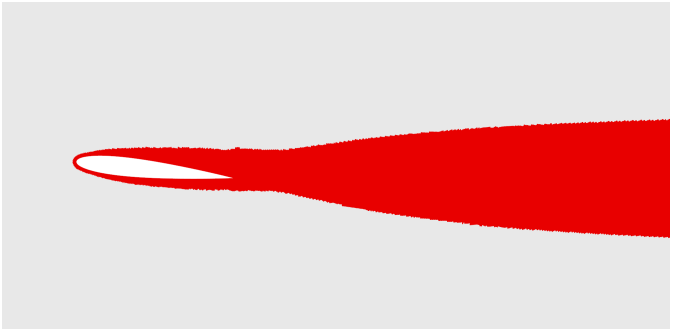

Figure 4.5: Viscous sensor δ_v^*.

Figures 4.7 and 4.8 display the results of the decomposition performed by varying the sensor and the downstream extension. The use of the sensor δ_v leads to an induced drag of the same order of magnitude as the viscous drag. Moreover, the various drag components exhibit very pronounced spikes. The most satisfactory result is obtained with the sensor δ_v^* and a downstream extension of 20 chords from the trailing edge. Therefore, all the results related to the drag decomposition and the comparison with the results derived from Toubin's formulation are based on the sensor described above.

Figure 4.6 shows the trends of the induced drag and the viscous drag.

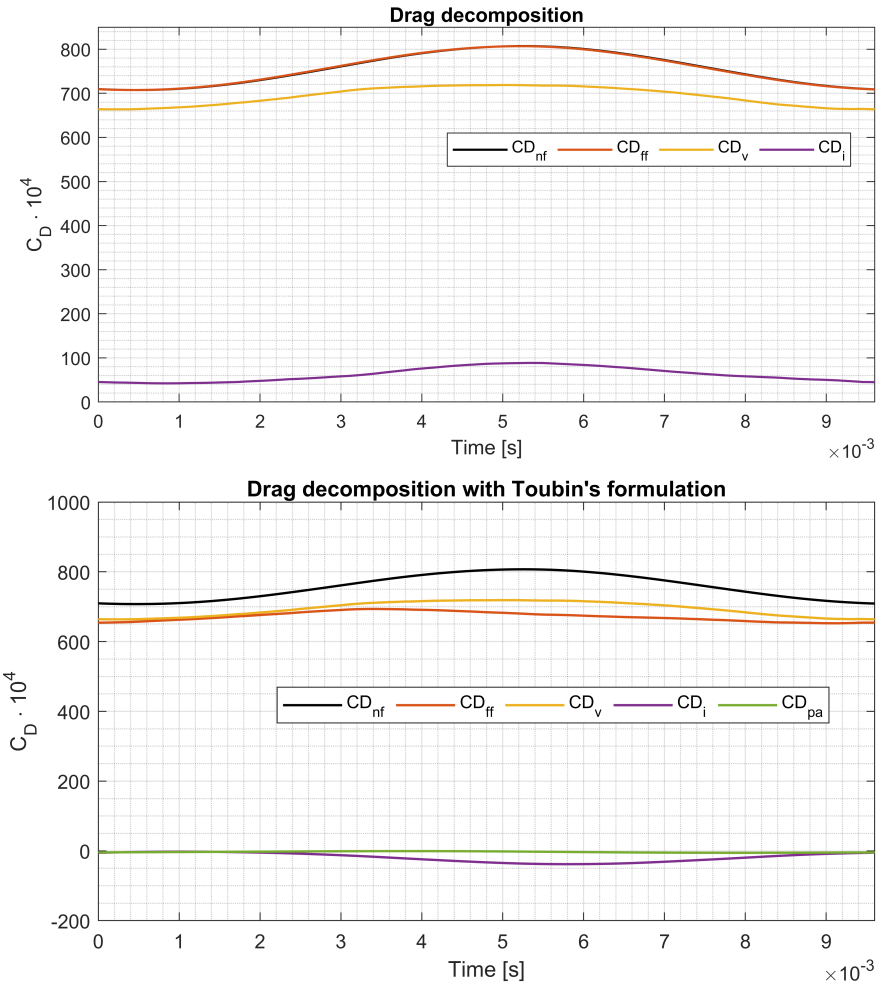

Figure 4.6: Drag decomposition.

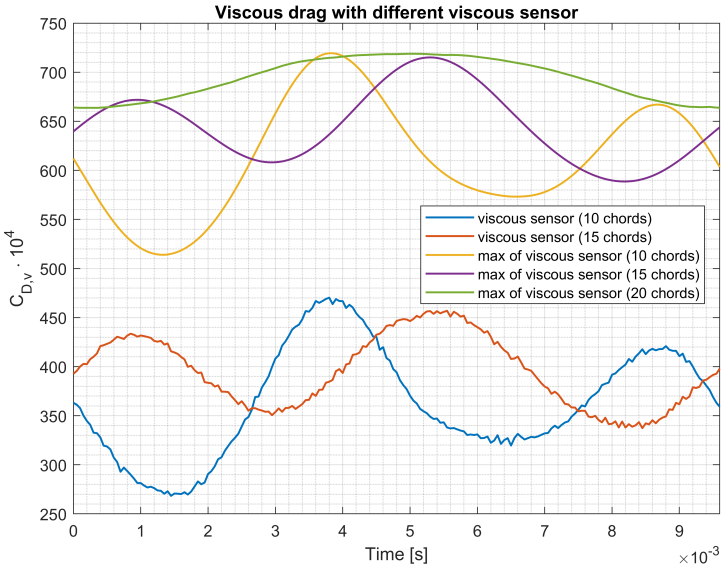

Figure 4.7: Viscous drag with different viscous sensors.

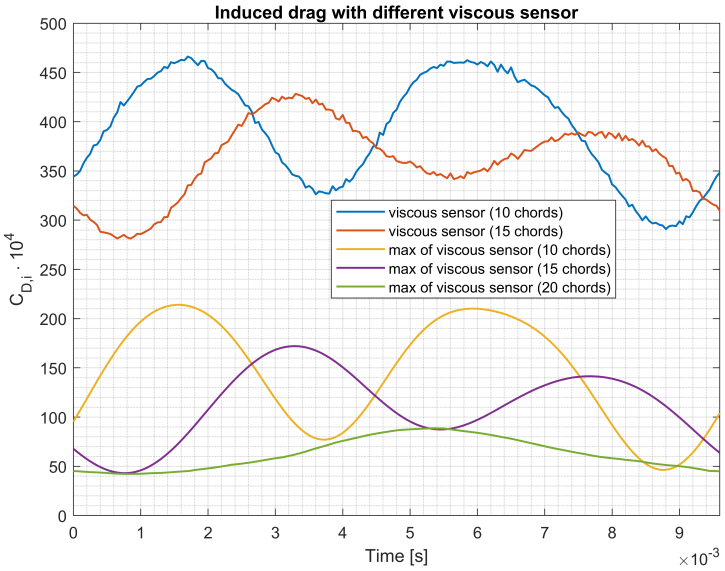

Figure 4.8: Induced drag with different viscous sensors.

4.2.1 Comparison with Toubin formulation

Over the same period, the decomposition is also performed using the formulation proposed by Toubin. The results are presented in figure 4.6. Bearing in mind that the definition of viscous drag is identical in both formulations, the only contributions to be compared are those of induced drag and acoustic drag.

In Toubin's formulation, the induced drag takes on negative values for almost the entire period analyzed, resulting in a discrepancy between the far-field drag and the near-field drag. The acoustic drag remains completely negligible, contributing less than 0.1% to the total drag. In figure 4.9, the induced drag and the square of the lift coefficient are compared between the formulation described in this work and Toubin's formulation.

The phase difference found in Toubin's induced drag may be due to the fact that there is a not negligible component of u_{irr} exiting the lateral surface of the viscous domain. This component is neglected in Toubin's formulation because of the assumption of streamtubes in the surface integral, but it is taken into account in the volume integral, which is fundamental to the phase.

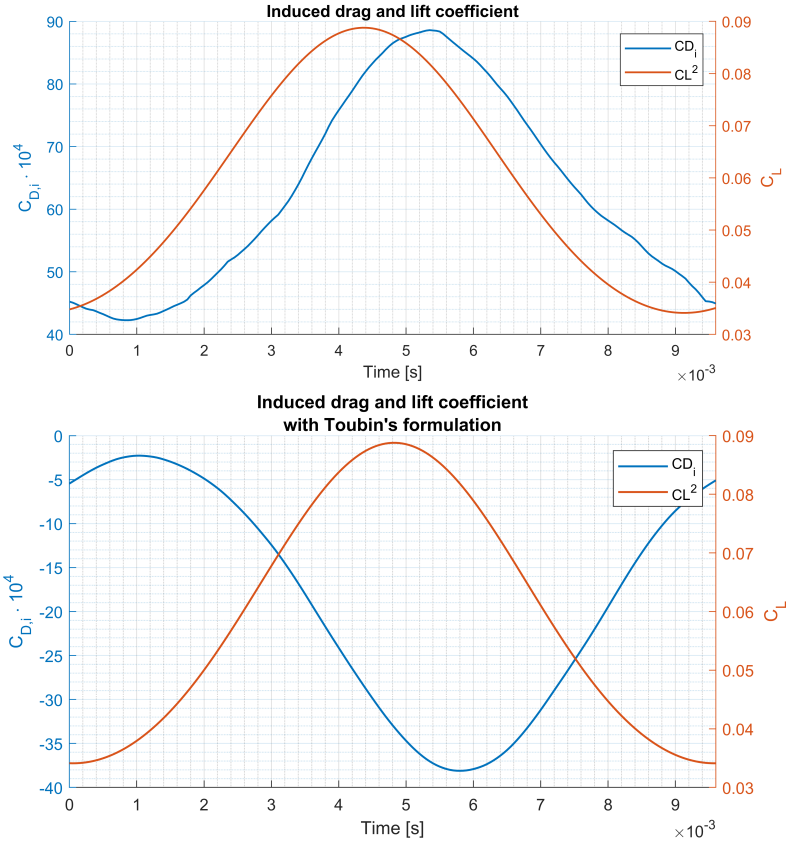

Figure 4.9: Induced drag compared to the square of lift coefficient in both formulations studied.

4.3 Turbulent vortex shedding

This two-dimensional simulation refers to a NACA0012 airfoil in stall conditions. The airfoil is set at an angle of attack $\alpha = 20°$ to the freestream direction, with $M = 0.2$ and $Re = 2 \cdot 10^6$. The numerical scheme is a third order of accuracy and it use Roe's scheme to compute the flux at the interfaces. The turbulence model for closure is the k-ω SST, with the standard value for realizability coefficient and the $a1$ blending function [8].

Several periods were analyzed over time, and the results shown refer to the last period calculated. The vortex shedding develops periodically, with a period $T = 2.62 \cdot 10^{-2}$ s. The time step used is $\Delta t = 5 \cdot 10^{-5}$ s.

During the first 20 periods, the viscous sensor was monitored, and all cells in which the viscous sensor was activated at least once were recorded. Based on this history of the viscous domain, a mesh refinement was performed on the domain to improve the efficiency of the solution in terms of computational resources. A polyhedral mesh was used, with 245522 cells, as shown in figure 4.10.

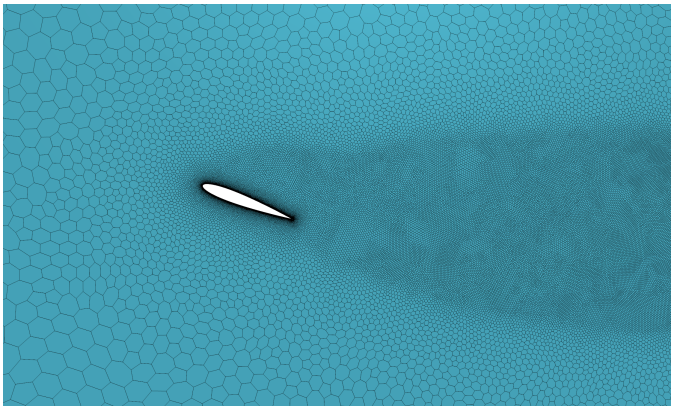

Figure 4.10: Mesh of vortex shedding case.

4.3.1 Results

Several periods were completed before analyzing the drag decomposition. As shown in figure 4.11, the vortex shedding is periodic and is subsequently transported by convective phenomena. The total drag coefficient reaches almost 5200 drag counts as a maximum and 3700 drag counts as a minimum.

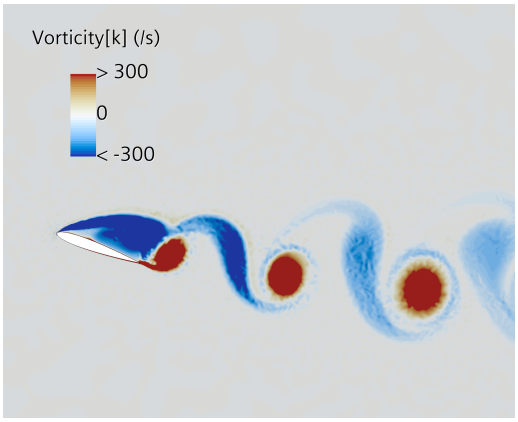

Figure 4.11: Z-component of vorticity.

Figure 4.12: Viscous domain definition.

Regarding the implementation of the drag decomposition method, there are extensive regions where the axial irreversible velocity u_{irr} is not defined. Nonetheless, it is possible to discern a pattern, since the separation bubble and the cores of the shed vortices are areas of low total pressure, as shown in figure 4.13. However, these regions are always included in the viscous domain and do not cause issues with the drag decomposition method.

Figure 4.13: Regions where u_{irr} is not defined. However, these regions are included in the viscous domain.

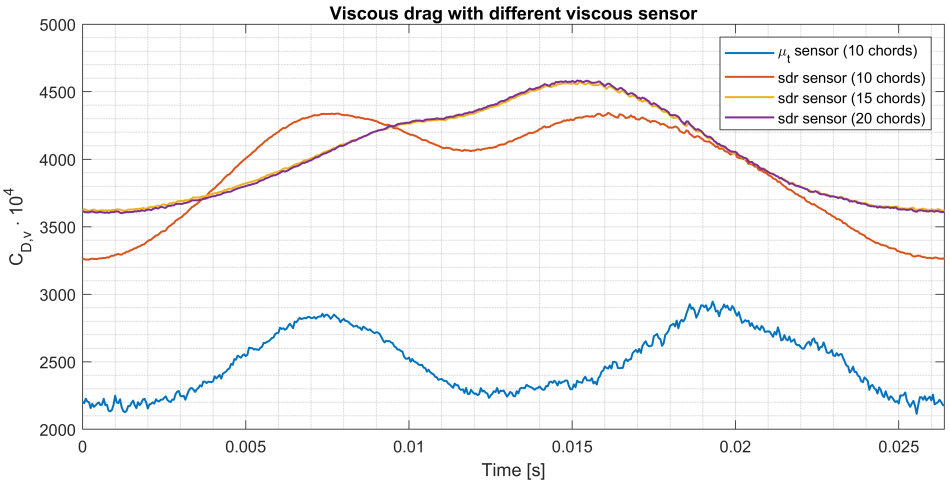

Figure 4.14: Viscous drag with different viscous sensors.

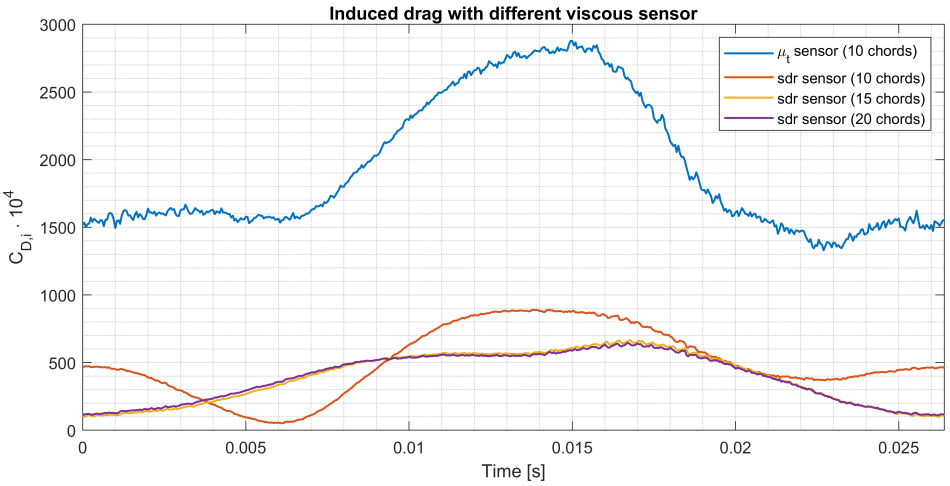

Figure 4.15: Induced drag with different viscous sensors.

Several viscous sensors were studied since the sensor (2.3) did not produce satisfactory results. The sensor used is based on the specific dissipation rate rather than the turbulent viscosity ratio and is

$$\delta_v = 1 \iff \begin{cases} \omega_t > k_{\omega_t} \\ ||\boldsymbol{S}|| > k_\tau \, \overline{\tau_w} \\ \delta_w = 0 \end{cases} \tag{4.1}$$

Another study was conducted on the downstream extension of the viscous domain. Initially tuned to 10 chords from the trailing edge (as indicated by the steady cases studies), it was extended to 15 and 20 chords, achieving a clear improvement in the decomposition and reaching a sort of convergence.

In figures 4.14 and 4.14, the trends of the viscous drag coefficient and the induced drag coefficient with the different sensors analyzed are shown. The chosen sensor was that defined by (4.1) and limited to 20 chords downstream of the trailing edge. The results of the drag decomposition are presented in figure 4.16.

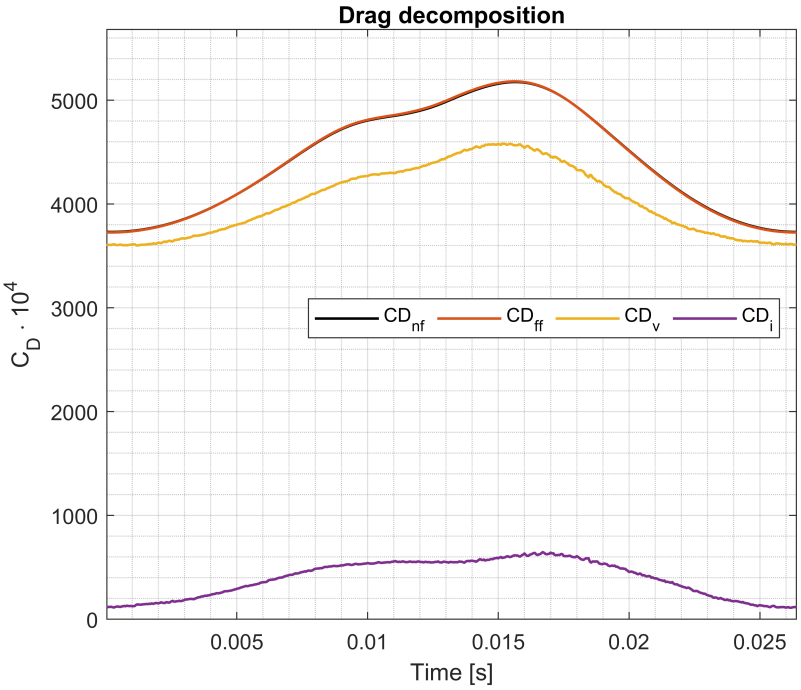

Figure 4.16: Results from drag decomposition. The biggest contribution is given by viscous drag, but there is an important induced drag.

In figure 4.17, the trend of the induced drag coefficient is shown alongside the square of the lift coefficient. The two trends do not seem to exhibit the same pattern. The induced drag appears to follow the drag coefficient more closely than the lift coefficient.

This may indicate that even the new sensor is not entirely capable of capturing the complete viscous phenomenon satisfactorily, resulting in a portion of it remaining in the complementary volume and being attributed to the induced drag.

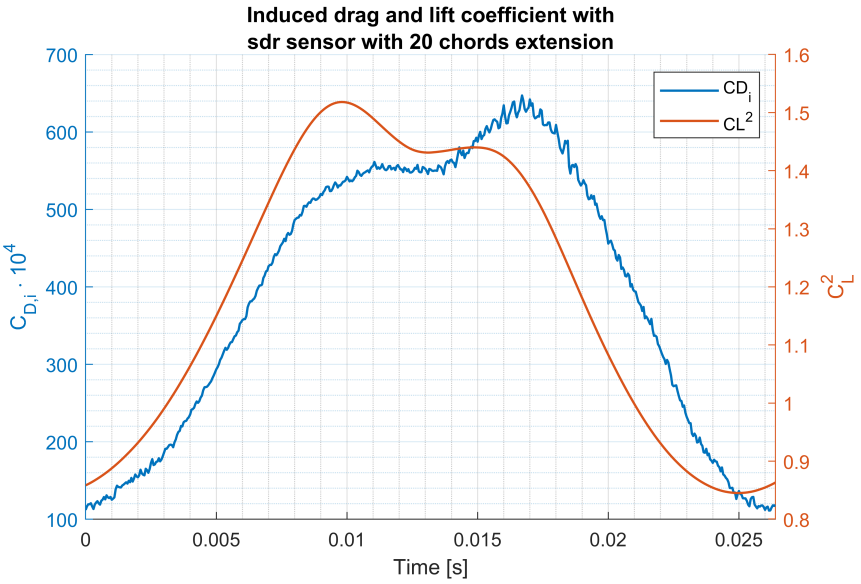

Figure 4.17: Comparison beetwen induced drag and the square of lift coefficient.

4.3.2 Comparison with Toubin formulation

In figures 4.18 and 4.19 the results obtained with Toubin's formulation are shown. The expression for the viscous drag is the same in both formulations, so it is interesting to compare only the induced drag.

It is immediately noticeable that the far-field drag does not perfectly match the near-field drag, with an error exceeding 9% at the maximum total drag point. The induced drag is limited to a maximum value of 190 drag counts, compared to a maximum value of 640 in the formulation used in this study.

The acoustic drag is very small, contributing less than 1% to the total drag and reaching a maximum value of -6 drag counts and a minimum of -40 drag counts.

However, a better correlation seems to exist when comparing the induced drag with the lift coefficient. In the analyzed period, the two peaks of the induced drag are better correlated with the lift coefficient than with the drag coefficient (with the first peak being greater than the second).

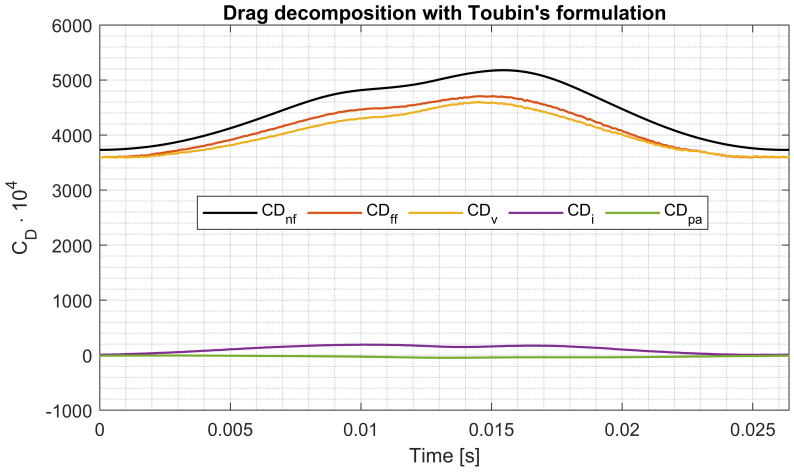

Figure 4.18: Results from drag decomposition with Toubin's formulation.

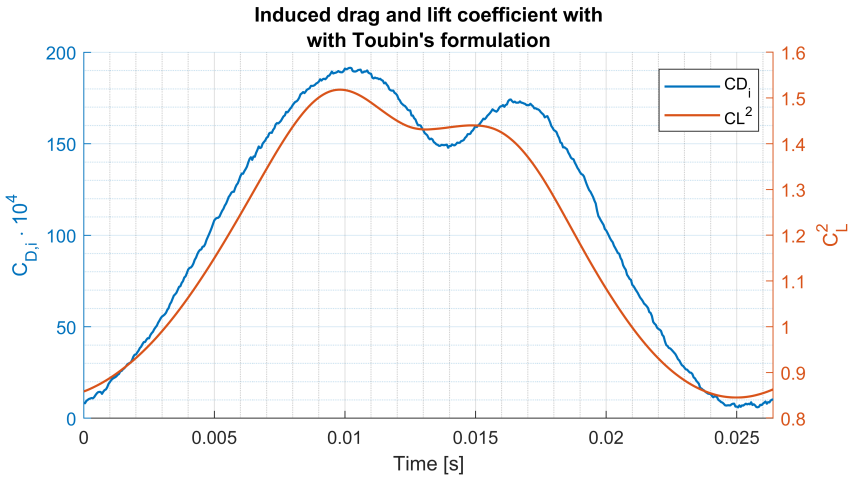

Figure 4.19: Comparison beetwen induced drag and the square of lift coefficient with Toubin's formulation.

4.4 Buffet case

In this simulation, the conditions analyzed by Brunet in [2] and recreated by Toubin [12]. The airfoil is a OAT15A model, a supercritical airfoil at an angle of attack $\alpha = 4.5$ deg to the freestream direction in transonic flow, with $M = 0.73$ e $Re = 3 \cdot 10^6$. The numerical scheme is a second order of accuracy and it use AUSM+ FVS scheme to compute the flux at the interfaces. The turbulence model for closure is the k-ω STT, with the standard value for realizability coefficient and the $a1$ blending function [8].

The chord is 1 m and the mesh has 620753 cells. A polyhedral mesh was used, with two different refinements: the first one based on the viscous sensor and the second one based on the shock sensor over several periods, to cover all positions of shock wave, as shown in figure 4.20.

The period of the oscillations is $T = 5.2 \cdot 10^{-2}$ s and the time-step used is $\Delta t = 7 \cdot 10^{-6}$ s. Several periods were analyzed over time, and the results shown refer to the last period calculated.

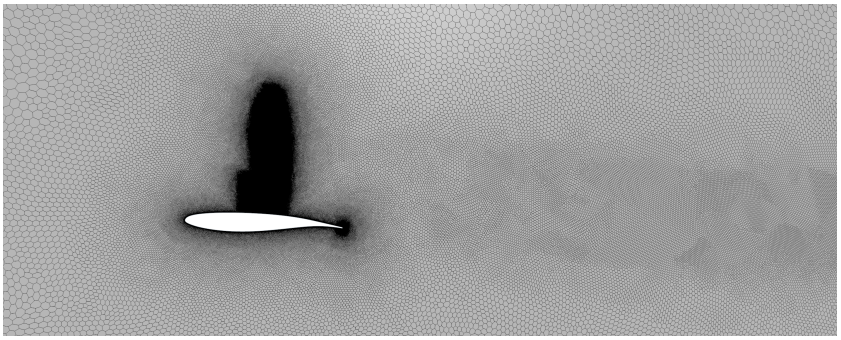

Figure 4.20: Mesh.

4.4.1 Results

Contrary to Toubin's studies in this specific case, the time evolution of the coefficients appears to be damped and seems to reach a steady solution. Other numerical schemes were tested, but none produced results similar to Toubin's. One possible reason could be the different preconditioner used in the unsteady solver. Further studies should be carried out. However, it is important to remember that our primary interest is in validating the drag decomposition rather than the accuracy of the simulations themselves.

The correlation between the near-field drag coefficient and the far-field drag coefficient is once again excellent, with the maximum error being less than 1%. The peak of the total drag does not coincide with the peaks of the individual drag components, which occur at different times, as shown in figure 4.24.

This case was interesting because, for the first time, it was possible to appreciate the contribution arising from the volume integral that encloses the wake of the shock wave. In particular, it can be observed that its contribution is very small compared to the others, but it is almost exactly out of phase, as shown in figure 4.25. As described by

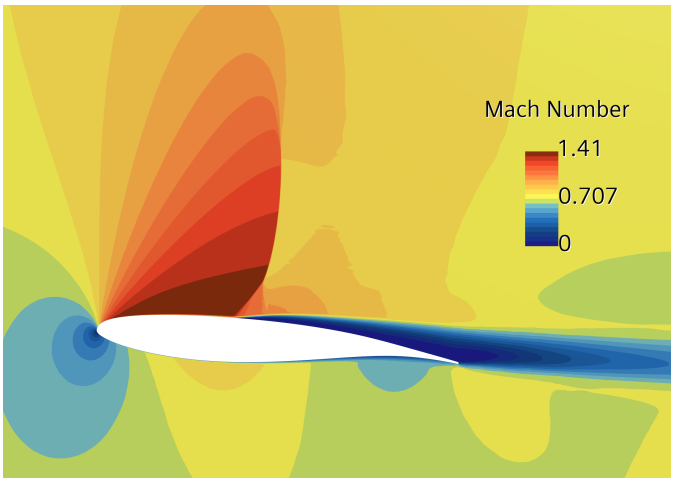

Figure 4.21: Mach number field.

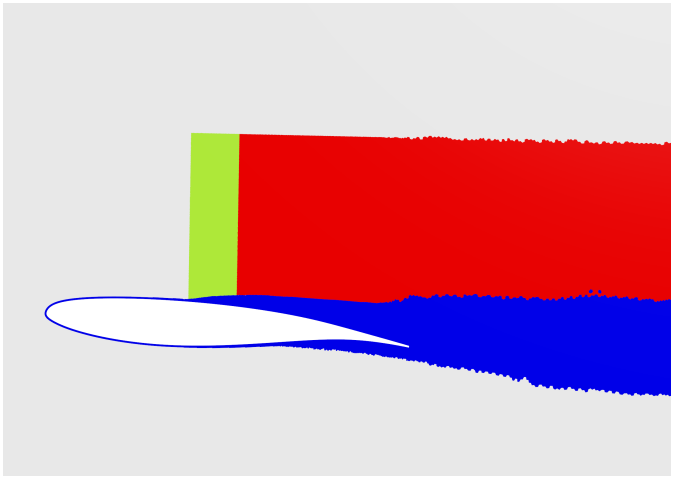

Figure 4.22: Viscous and wave domains definition.

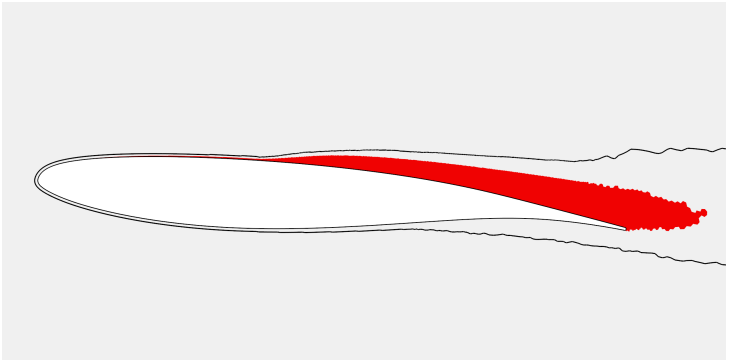

Figure 4.23: Regions where u_{irr} is not defined. However, these regions are included in the viscous domain, as shown with the black line.

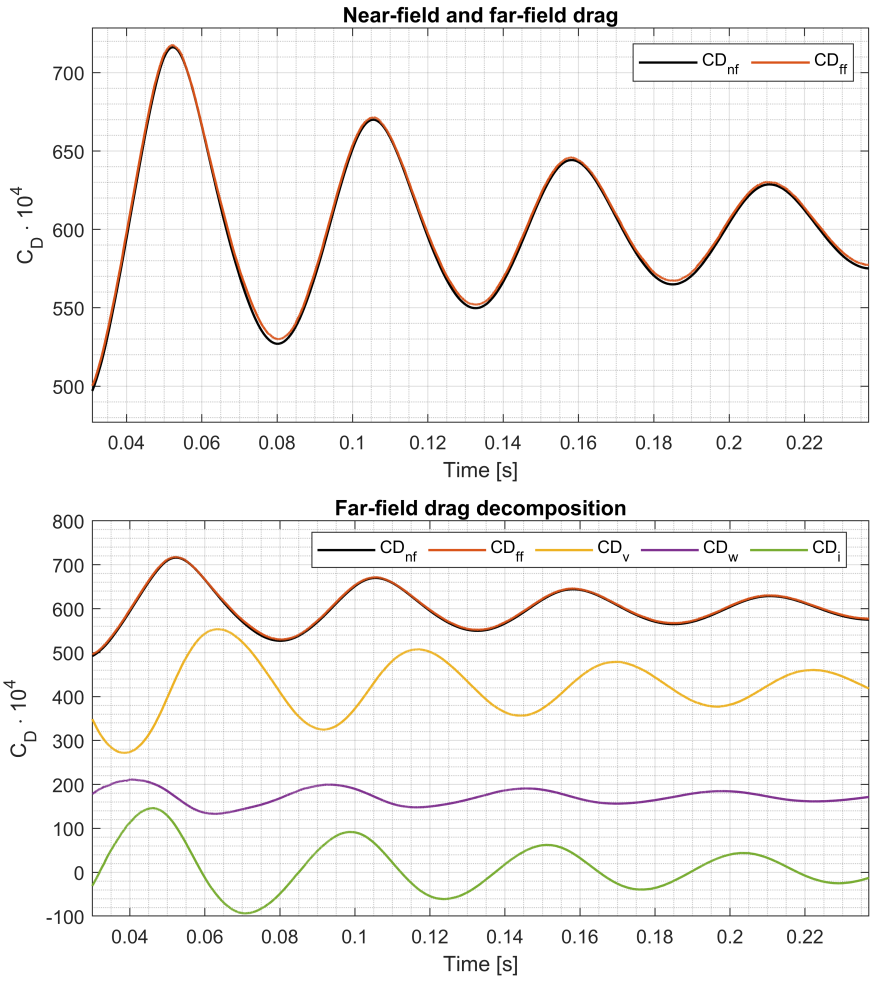

Figure 4.24: Drag decomposition result for buffet case.

Table 4.1: Values from drag decomposition for the most forward and backward position of the shock. Toubin's data were interpolated from his plots.

	C_L	C_D	$C_{D,ff}$	$C_{D,v}$	$C_{D,w}$	$C_{D,i}$
Highest C_D (this study)	1.04	716	718	440	173	103
Lower C_D (this study)	0.830	492	497	343	178	-31
Highest C_D (Toubin)	/	780	760	430	220	100
Lower C_D (Toubin)	/	490	470	320	230	-70

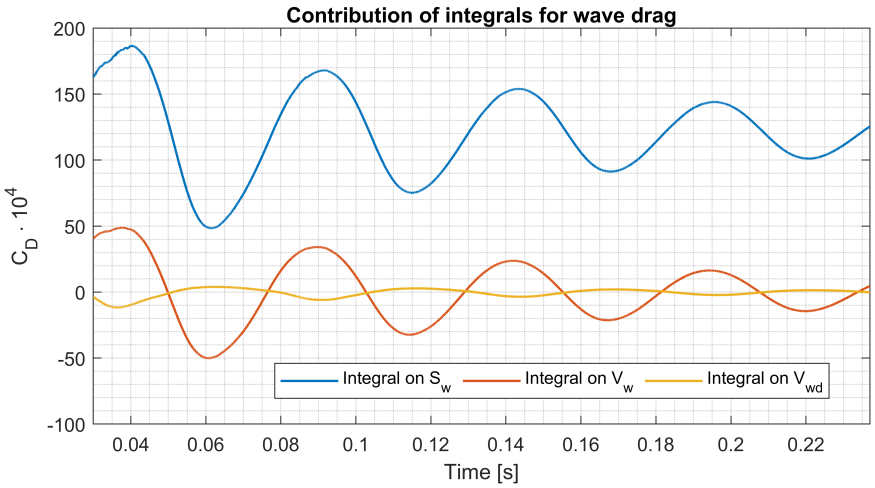

Figure 4.25: Contribution of wave integral terms.

Toubin herself, this contribution serves to eliminate the delay in the signal, created by performing the surface integral closer to the shock (where refinement is already in place) and to reduce numerical integration errors.

Another key aspect is that a non-negligible induced drag component was found in a two-dimensional simulation. This contribution is due both to the part of f_{irr} that was not included in the viscous or shock domain and to a component arising from f_{rev} in the entire complementary domain. In figure 4.26, the trend of the induced drag coefficient with respect to the square of the lift coefficient is shown. The sinusoidal and damped behavior is present in both cases, although there is a small delay between the two trends.

This delay is also observed in Toubin's studies, but it may not be coincidental. In fact, the time interval between the peak of $C_{D,i}$ and that of C_L^2 is $\Delta t \sim 3.5 \cdot 10^{-3}$ s, which is comparable to the characteristic time $t_c = c/V_\infty \sim 4 \cdot 10^{-3}$ s.

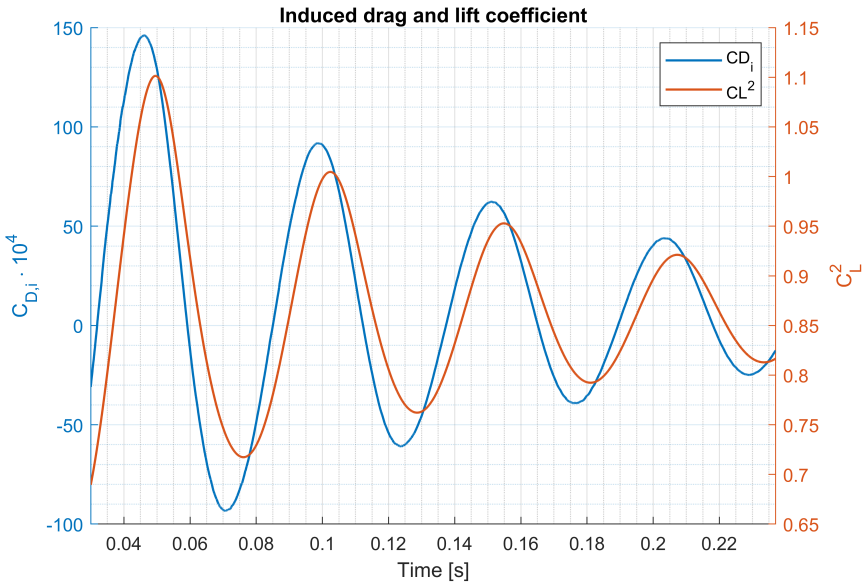

Figure 4.26: Induced drag coefficient and the square of the lift coefficient in time.

The main contribution to the induced drag in this case study is, however, due to the f_{irr} component in V_c. It is reasonable to raise some doubts regarding the definition of the integration domains, which should be evaluated in future studies.

4.4.2 Comparison with Toubin formulation

In figure 4.27, the trends of the viscous, wave, and induced drag obtained using Toubin's formulation are shown. The induced drag has an amplitude not very different from that obtained with the formulation used in this study. However, it exhibits a significant phase shift, resulting in a far-field drag that is out of phase with the near-field drag. Moreover, the acoustic component is very low, contrary to Toubin's study [12], where the acoustic component contributes more than 20%.

In figure 4.28, the trend of the induced drag and the square of the lift coefficient is shown, which changes due to the movement of the shock wave and the resulting separation point. The two trends are almost in quadrature, highlighting a poor handling of the temporal derivatives, whose role is to cancel out the delay between the far-field drag and the near-field drag.

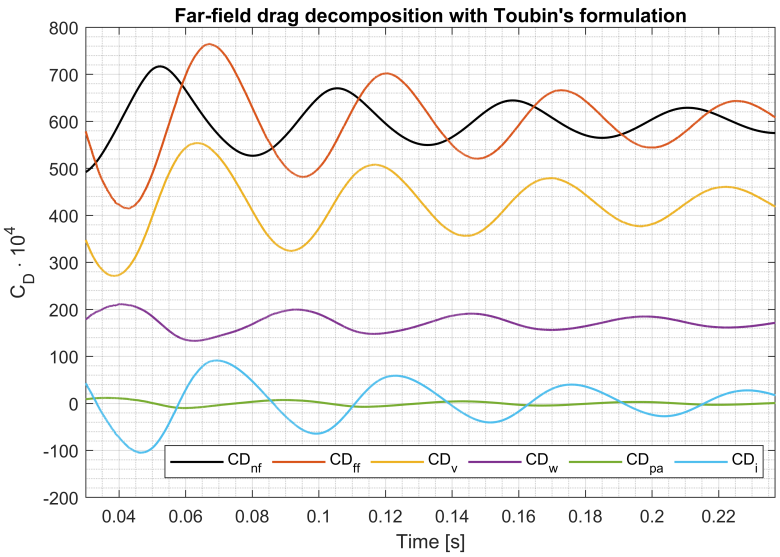

Figure 4.27: Drag decomposition with Toubin's formulation.

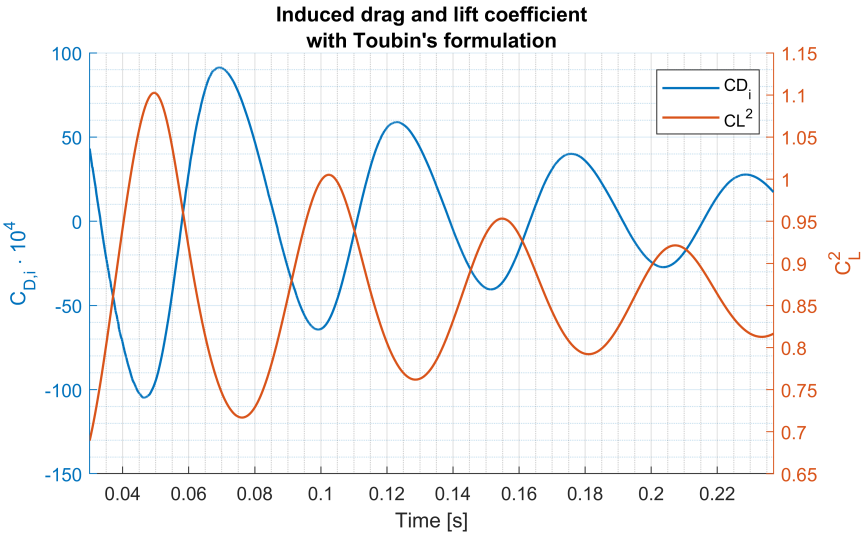

Figure 4.28: Comparison between induced drag and the square of the lift coefficient with Toubin's formulation.

4.5 Inviscid flow over an airfoil with heaving motion

The last case study concerns a two-dimensional airfoil immersed in an inviscid, subsonic flow, which undergoes a heaving motion in the direction perpendicular to the freestream flow. The airfoil is a NACA0012 positioned at an angle of attack $\alpha = 0°$ and is subjected to a flow with Mach number $M_\infty = 0.2$. A heaving motion is applied throughout the domain, following the law

$$v(t) = A\, sin(2\,\pi\, f\, t)$$

and where it was set $A = 0.144\, M_\infty$ e $f = 20$ Hz.

Now, there is an additional velocity component due to the motion of the domain, and it must be taken into account in the balance (1.2). Since there are no accelerations along the direction parallel to the flow, the balance equation becomes [4]

$$D_{ff}(t) = \int_{S_e} (\mathbf{f_r} \cdot \mathbf{n})\, \mathrm{d}S - \int_{S_a} \rho(u - u_\infty)(\mathbf{q_r} \cdot \mathbf{n})\, \mathrm{d}S - \int_V \frac{\partial \rho(u - u_\infty)}{\partial t}\, \mathrm{d}V \tag{4.2}$$

where

$$\boldsymbol{f_r} = -\rho(u - u_\infty)(\mathbf{q_r} \cdot \mathbf{n}) - (p - p_\infty)(\mathbf{i} \cdot \mathbf{n}) + (\boldsymbol{\tau}_x \cdot \mathbf{n})\,.$$

Developing the decomposition of the relative velocity

$$\mathbf{q_r} = \mathbf{q} - \mathbf{q_{grid}}$$

and comparing the two balance equations (1.2) and (4.2), an additional term is found that must be present in the balance equation, and it is

$$\int_{S_e} \rho(u - u_\infty)\, \mathbf{q_{grid}} \cdot \mathbf{n}\, \mathrm{d}S + \int_{S_a} \rho(u - u_\infty)(\mathbf{q_{grid}} \cdot \mathbf{n})\, \mathrm{d}S = \int_V \nabla \cdot [\rho(u - u_\infty)\mathbf{q_{grid}}]\, \mathrm{d}V\,.$$

This term accounts for the axial momentum flux over the entire domain that varies because the domain itself is moving. It should be noted that this term is identically equal to D_m. For this initial analysis, this contribution was assigned to the volume integrals related to the induced drag.

In addition, it was necessary to modify the boundary condition in the inflow region of the domain. The stagnation inlet boundary condition requires a velocity field that aims inside the domain. When the heaving velocity was at its maximum this does not happen. So, it was decided to apply the freestream boundary condition, rather than a stagnation inlet and pressure outlet.

4.5.1 Results

This case is interesting for two reasons. The first is the opportunity to analyze the drag component due to the motion of a body, which is already implemented in Toubin's model. The second is that the only other drag component is due to induced drag, since there are no viscous effects and no shock waves are formed.

In the period $T = 1/f = 0.05$ s, the near-field drag coefficient exhibits two negative peaks and two nearly zero minima, while the lift coefficient shows one positive maximum and one negative maximum. The mesh used for the analysis consists of 382528 polyhedral cells. Since no sensor is defined in this case study, the refinement along the wake is uniform and is defined by a rectangular box with a downstream extension of 20 chords from the trailing edge. A layer of prism cells was added to ensure good orthogonality near the wall.

Furthermore, a second, finer refinement is created around the airfoil using a surface offset, as shown in figure 4.30.

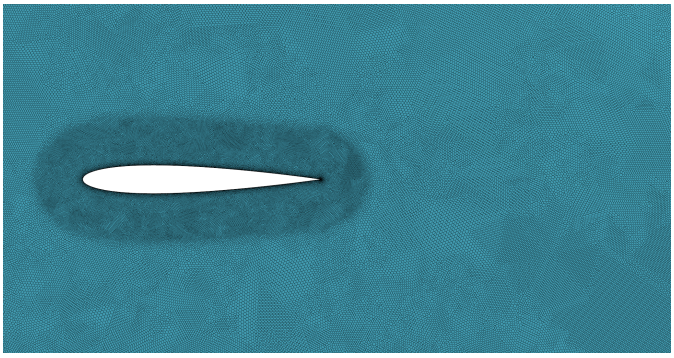

Figure 4.29: Computational grid.

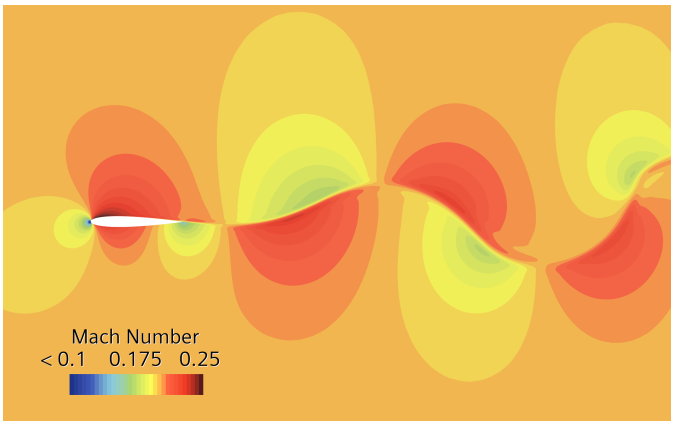

Figure 4.30: Mach number field in the motion case.

The results of the drag decomposition are shown in figure 4.31. It can be observed that this is the only case study in which the momentum balance is not perfect. In fact, the far-field drag coefficient does not follow the drag coefficient curve near its minimum points, which correspond to the minimum velocity points of the airfoil.

The induced drag and the motion drag are slightly out of phase with the far-field drag. In figure 4.31, the trends of the induced drag and the square of the lift coefficient

during the period are also presented. As in all the other cases analyzed previously, the two behaviors are consistent and a phase difference is present between the two quantities.

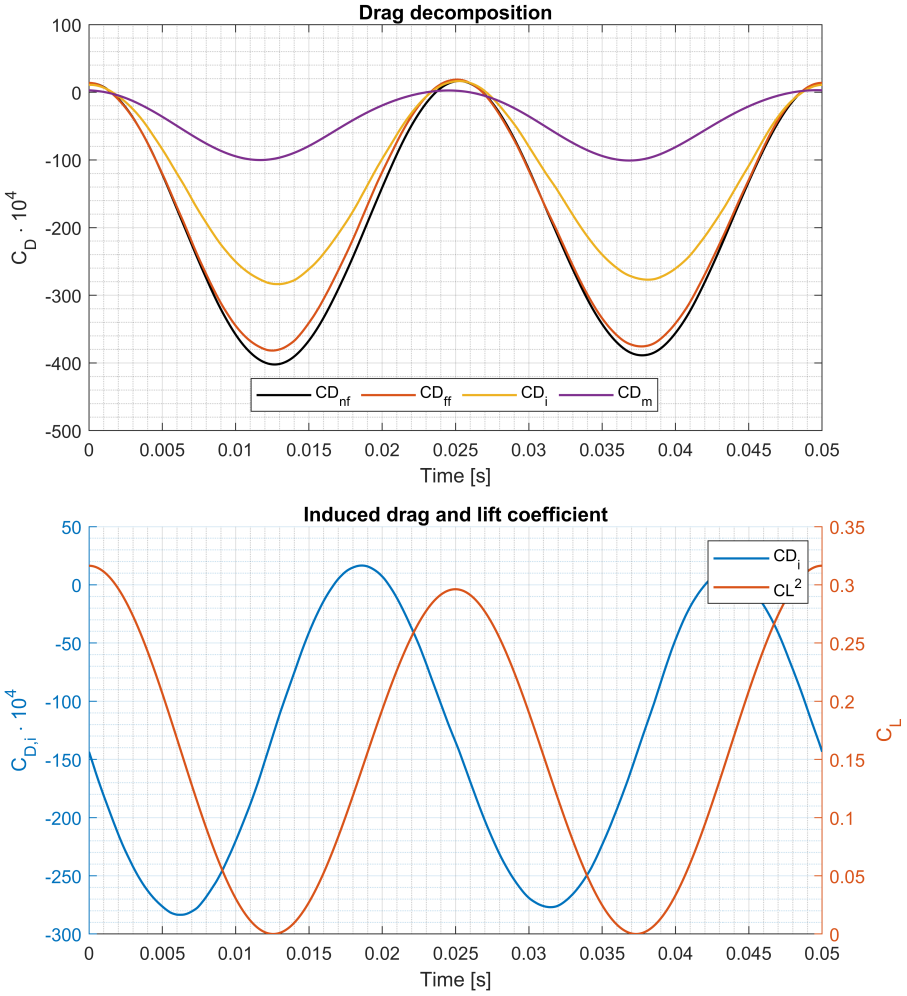

Figure 4.31: Drag decomposition result and comparison between induced drag and the square of lift coefficient.

4.5.2 Comparison with Toubin formulation

The volume term arising from the use of the relative velocity $\boldsymbol{q_r}$ has been included in the expression for the induced drag in Toubin's formulation. In Figure 4.32, the results of the drag decomposition are shown. It is immediately noticeable that the induced drag behaves completely incorrectly compared to the other drag components, even though it follows the trend of the square of the lift coefficient.

One of the reasons for this lies in the assumption made by Toubin in her study [12], where he assumes that there is no temporal variation of entropy in the entire complementary volume $V_c \equiv V$. This assumption turns out to be incorrect in this case, as shown in figure 4.33.

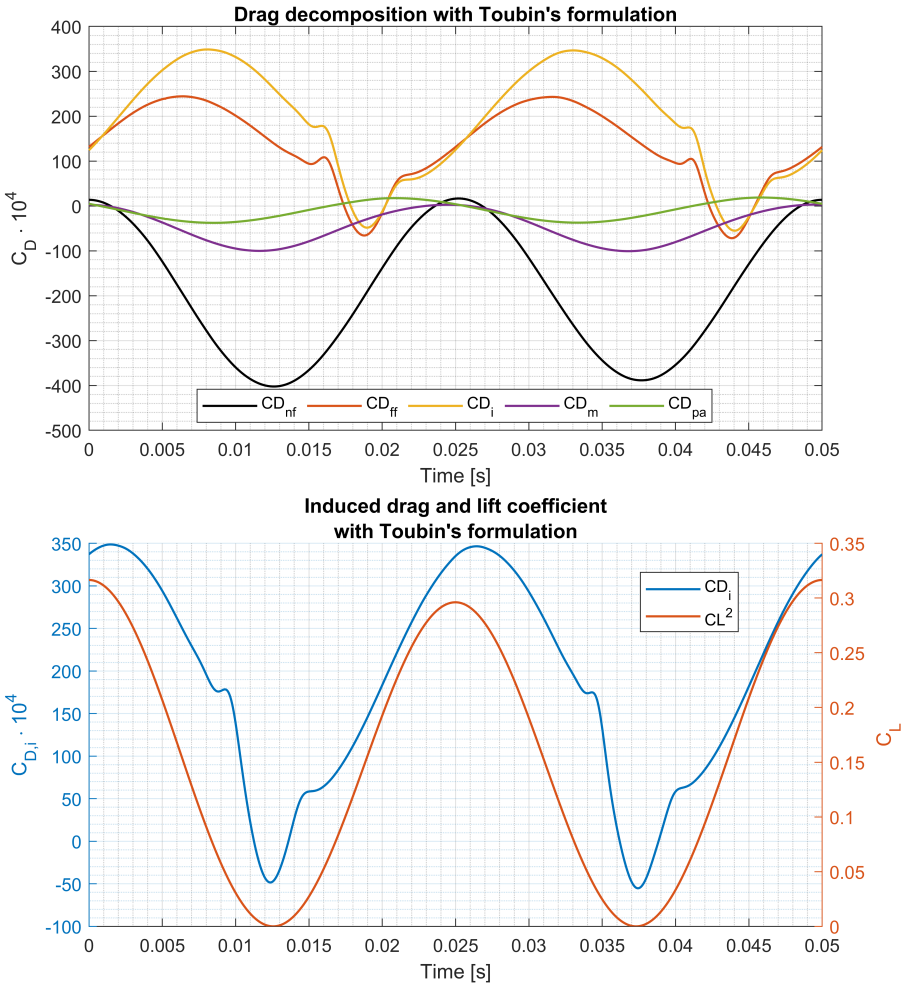

Figure 4.32: Drag decomposition result and comparison between induced drag and the square of lift coefficient with Toubin's formulation.

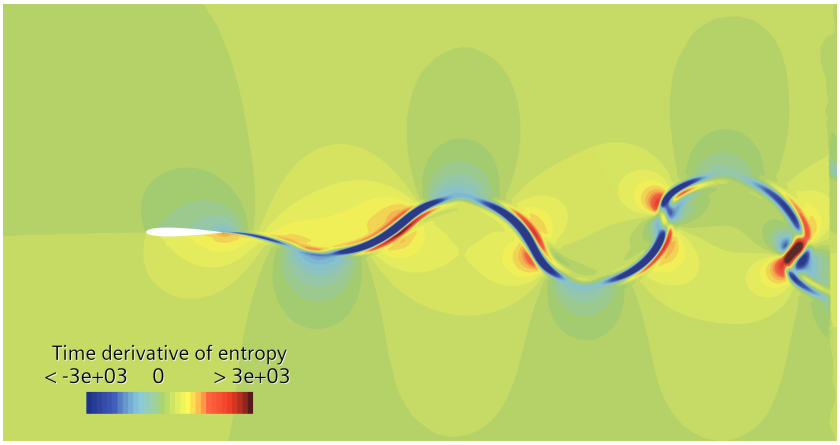

Figure 4.33: Time derivative of entropy along the contact surfaces.

Chapter 5

Conclusion

In all the case studies conducted in this work, a formulation based on the division of the control surfaces and volumes defined in the balance equation (1.2) has been used. With this formulation, a very strong correlation was achieved between the near-field drag and the far-field drag, compared to the formulation adopted by Toubin in her studies [12].

However, one note must be made. Although the viscous and wave drag are calculated in the same way as adopted by Toubin, the induced drag is computed as the complementary part resulting from the balance equation (1.2). This solution does not allow a physical definition of the induced drag, in which spurious contributions could be present due to an imperfect definition of the wave and viscous domains. In fact, while the definition of the wave and viscous domains does not affect the induced drag as defined by Toubin, it remains an important element in the formulation used in this work. In particular, the induced drag defined in (1.7) contains a surface integral over the boundary of the complementary volume, which is in turn defined by the wave and viscous sensors.

Nevertheless, the case of a moving airfoil in an inviscid flow remains unaffected by this discussion. In this case, the error committed by Toubin's formulation is not due to the definition of the domains, since the complementary volume coincides with the entire computational domain. The assumption that $Ds/Dt = 0$ in V_c is not satisfied, and the decomposition of the unsteady induced drag (1.7) into induced and acoustic drag is not valid.

The steady cases performed were useful for gaining a better understanding of the definition of the domains using sensors. In particular, the most important results were:

- The viscous domain is strongly influenced by the downstream extension and the cell quality. In the case of an unstructured mesh, the viscous domain must fall within the refined area, at least extending 10 chords from the airfoil.
- The use of a sensor to detect the shock wave is reasonable. However, the definition of a box that encloses the sensor improves the accuracy of the surface integral calculation, by avoiding integration in proximity to the shock, where strong gradients are present.

The unsteady cases give a very different result. In particular:

- The sensors defined by Toubin [12] did not lead to satisfactory results in the studied cases where large-scale turbulent structures are developed along the wake.
- New sensors were defined, yielding satisfactory results only when their downstream extension was increased to more than 15–20 chords.

In summary, the formulation adopted in this study yields excellent results regarding far-field drag. However, the induced drag is defined as the complementary part of the far-field drag calculated via the balance equation (1.2). In contrast, Toubin's approach aims for a dedicated definition of induced drag and its further decomposition into additional phenomena. Nevertheless, applying Toubin's formulation requires further research on the sensors used to define the integration volumes, since using domains that are not streamtubes introduces an intrinsic error into the formulation. In fact, the use of Toubin's formulation with domains that are not streamtubes creates a mismatch between surface and volume integrals; the flux on the lateral surfaces is neglected, but the time variation is accounted for in the volume integral.

Bibliography

[1] Albert Betz. A method for the direct determination of wing-section drag. Technical report, 1925.

[2] Vincent Brunet. Computational study of buffet phenomenon with unsteady rans equations. In *21st AIAA Applied Aerodynamics Conference*, page 3679, 2003.

[3] D Destarac and JJAs Van Der Vooren. Drag/thrust analysis of jet-propelled transonic transport aircraft; definition of physical drag components. *Aerospace science and technology*, 8(6):545–556, 2004.

[4] Martin Gariepy, Jean-Yves Trepanier, and Benoit Malouin. Generalization of the far-field drag decomposition method to unsteady flows. *AIAA journal*, 51(6):1309–1319, 2013.

[5] Charles D Harris. Two-dimensional aerodynamic characteristics of the naca 0012 airfoil in the langley 8 foot transonic pressure tunnel. Technical report, 1981.

[6] Cambridge University Aeronautics Laboratory. *Measurement of profile drag by the pitot-traverse method*. HM Stationery Office, 1936.

[7] EC Maskell. Progress towards a method for the measurement of the components of the drag of a wing of finite span. *RAE Technical Report No. 72232*, 1972.

[8] Nasa. Turbulence modeling resource, 2019.

[9] Klaus Oswatitsch, Gustav Kuerti, and CM Ablow. Gas dynamics. vol. 1 of applied mathematics and mechanics. *Physics Today*, 10(7):30–32, 1957.

[10] Luigi Paparone and Renato Tognaccini. Computational fluid dynamics-based drag prediction and decomposition. *AIAA journal*, 41(9):1647–1657, 2003.

[11] Alessio Raffa. *Implementation and Analysis of Far-Field Methodologies for Aerodynamic Force Decomposition in a Comercial CFD Software*. PhD thesis, Politecnico di Torino, 2023.

[12] Hélène Toubin and Didier Bailly. Development and application of a new unsteady far-field drag decomposition method. *AIAA Journal*, 53(11):3414–3429, 2015.

[13] JZ Wu and JM Wu. Vortical sources of aerodynamic force and moment. Technical report, SAE Technical Paper, 1989.